The Pennsylvania State University

The Graduate School

RELATIONSHIP BETWEEN HUMAN ACHILLES TENDON MOMENT ARM AND PLANTARFLEXOR MUSCLE ARCHITECTURE

A Thesis in

Kinesiology

by

Logan Faux-Dugan

Submitted in Partial Fulfillment
of the Requirements
for the Degree of

Master of Science

December 2022

The thesis of Logan Faux-Dugan was reviewed and approved by the following:

Stephen J. Piazza
Professor of Kinesiology
Thesis Adviser

Jonas Rubenson
Associate Professor of Kinesiology

John Challis
Professor of Kinesiology

Jonathan B. Dingwell
Professor of Kinesiology
Graduate Program Director

ABSTRACT

Sufficient plantarflexor muscle moment is critical to locomotor function, so the direct determinants of this moment, plantarflexor force, and the plantarflexor moment arm of the Achilles tendon (ATMA), are also of great importance. The primary plantarflexor muscles – the lateralis gastrocnemius (LG), medialis gastrocnemius (MG), and soleus – transmit force through the Achilles tendon (AT) to generate a plantarflexion moment about the ankle as the foot pushes off from the ground during locomotion. The plantarflexor moment may be thought of as the product of the AT force and the ATMA, which determines the leverage of the AT force about the ankle joint axis. Muscle architecture parameters – such as fascicle length (FL), pennation angle (PA), muscle volume (MV), and physiologic cross-sectional area (PCSA) – influence plantarflexor force through the force-length (F-L) and force-velocity (F-V) properties of muscle. Several recent studies have reported differences in the relationships between ATMA and plantarflexor architecture between groups with different functional demands (e.g., sprinters and non-sprinters) and associations have been found between ATMA and functional capacity in terms of energetic efficiency during distance running. The purpose of this thesis was to investigate the relationship between ATMA and architecture of plantarflexor muscles (LG and MG) in a healthy, adult, non-athlete population. Therefore, measurements were taken of the ATMA and architecture (FL, PA, MV, & PCSA) of the LG and MG. Significant positive correlations were observed between ATMA and LG fascicle length, MG PCSA, and MVs of the LG and MG, and there are implications for these associations. With all else equal, a larger ATMA increases muscle contraction velocity which decreases muscle force according to the F-L and F-V properties. Although this research cannot answer questions about the cause of these associations, it is possible that larger fascicle lengths, PCSAs, and muscle volumes of the plantarflexors might reduce the force lost from the larger ATMA. Future studies should investigate the relationship between ATMA and plantarflexor architecture in different populations to see if similar relationships exist.

TABLE OF CONTENTS

LIST OF FIGURES

LIST OF TABLES

ACKNOWLEDGEMENTS

I would like to acknowledge my wife and family for supporting me throughout this process. Also, thank you to Steve Piazza. I could not have asked for better support from you all.

Funding was received from the College of Health and Human Development for this thesis. Findings and conclusions of this work do not necessarily reflect the view of the funding agency.

Chapter 1

Introduction

1.1 Background

Plantarflexor force and the plantarflexor moment arm of the Achilles tendon (ATMA) are critical to locomotor function. The triceps surae muscles – the lateralis gastrocnemius (LG), medialis gastrocnemius (MG), and soleus (SOL) – insert on the Achilles tendon (AT) which, in turn, inserts onto the posterior calcaneus. These muscles transmit force through the AT to generate a plantarflexion moment about the ankle during locomotion. Mathematically, a plantarflexion moment is equal to the product of the AT force and ATMA. This plantarflexion moment is opposed by the moment determined by the ground reaction force (GRF) and its moment arm about the ankle. The moment arm of the GRF can be much greater than the ATMA, putting the plantarflexors at a mechanical disadvantage. Despite this mechanical disadvantage, locomotion is achieved through an intricate interplay between architectural factors that contribute to muscle-tendon unit (MTU) force and joint tendon moment arm.

Muscle architecture influences MTU force through the force-length (F-L) and force-velocity (F-V) relations. Muscle architecture refers to the size and arrangement of fibers within a muscle and is defined by parameters such as optimal fiber length, pennation angle, and muscle size parameters such as muscle volume and physiological cross-sectional area (PCSA). Optimal fiber length corresponds to when the average sarcomere length is positioned on the plateau region of the F-L curve whereby maximum tetanus tension is achieved, and this parameter determines where muscle operates on the F-L curve (Lieber & Fridén, 2000). To maximize the force generated for joint motions necessary for locomotion, fiber length (serial sarcomere length)

excursions should oscillate about the optimal fiber length. The parameter optimal fiber length affects the force generating capacity and shortening velocity of sarcomeres by determining operating range on the F-L and F-V curves (Lieber & Fridén, 2000). Pennation angle, the acute angle between the fibers and aponeuroses, allows shorter fibers to be packed in parallel and thus influences force production and operating point on the F-L and F-V curves as well (Gans, 1982; Lieber & Ward, 2011). Additionally, muscle size, or the amount of contractile material in a muscle, has an impact on force generating capacity (Gans, 1982; Lieber & Ward, 2011). Several studies have indicated positive correlations of force generating capacity with muscle volume (Baxter & Piazza, 2014; Blazevich et al., 2009; Fukunaga et al., 2001) and PCSA (Bamman et al., 2000; Lieber & Fridén, 2000; Lieber & Ward, 2011).

Interactions between muscle architectural parameters and ATMA influence production of the plantarflexor moment needed for locomotion (Lee & Piazza, 2009). Although a shorter ATMA reduces leverage, it may also reduce muscle shortening velocity and thus increase muscle force-generating capacity, especially during rapid joint rotations. Nagano and Komura (2003) used computer simulations to show that shorter ATMAs result in greater joint moment, power, and work for fast ankle plantarflexions. Additionally, Baxter and Piazza (2014) observed in individuals with shorter ATMAs that ankle joint moment declines to a lesser degree at high speeds of joint rotation, which supports earlier observational data (Lee & Piazza, 2009). Lee and Piazza (2009) found shorter ATMAs and longer fascicles in the LG of sprinters when compared with non-sprinters; through simulations investigating this structure-function relationship, it was suggested that the mechanical leverage lost by having a short ATMA was compensated by operating on a more favorable region on the F-L and F-V curves of muscle (Lee & Piazza, 2009). Additionally, knee extensor moment arm has also been positively correlated with sprinting and long-distance

running performance (Miyake et al., 2017; Tomita et al., 2018). This background suggests there are specific mechanisms within different joint systems which use the F-L and F-V relations to produce locomotion.

Recent studies have identified relationships between muscle architecture and tendon moment arm across joint systems (Hori et al., 2020; Maden-Wilkinson et al., 2020; Maganaris et al., 2006; Sugisaki et al., 2010; Sugisaki et al., 2015). In the elbow joint, (Sugisaki et al., 2010) found a positive correlation between triceps brachii tendon moment arms and anatomical cross-sectional area (ACSA) of the triceps brachii. These researchers also observed a slight increase in triceps brachii tendon moment arm after resistance training-induced hypertrophy (increased ACSA) of the triceps brachii (Sugisaki et al., 2015). Additionally, Hori et al. (2020) found that knee extensor moment arms are positively correlated with force producing capacity, which is defined as knee extensor peak isometric moment divided by quadriceps femoris muscle volume.

Further, in the ankle it appears that ATMA length is load dependent and, potentially, related to muscle volume but not fascicle length. Rasske and Franz (2018) reported that ATMA increases with plantarflexion during walking, as triceps surae muscle bulging increases. This load dependent increase in ATMA tends to be more pronounced in younger subjects when compared with elderly subjects who may have sarcopenia (Rasske & Franz, 2018). Additionally, Baxter and Piazza (2014) found a near significant relationship between triceps surae muscle volume and ATMA. This relationship between muscle size and ATMA further suggests there could be size effects that impact MTU leverage. However, finally, Maganaris et al. (2006) found weak correlations between fascicle length and tendon moment arm within the plantarflexors (LG, MG, and SOL) and knee extensors (vastus lateralis and vastus intermedius).

Still, there are relatively few direct investigations of the relationship between ATMA and plantarflexor muscle architecture, especially within a young adult, healthy, non-athlete population. Filling this gap in our knowledge could help us better understand the role of musculoskeletal structure within non-athletic populations. Knowledge of these structure-function relationships could help create clinical protocols that help aging populations, as they tend to lose plantarflexor leverage and muscle tissue as they age (Kim et al., 2011).

1.2 Specific aims, hypotheses, predictions, and rationales

The purpose of this study was to evaluate the correlations between ATMA and plantarflexor muscle architecture. The following specific aims are proposed:

1. Test and implement 3D ultrasound (3DUS) for measuring muscle volume.
2. Recruit untrained, healthy, skeletally mature individuals to measure their ATMAs and the following muscle architecture parameters in the plantarflexors LG and MG: fiber length, pennation angle, and muscle size (muscle volume and PCSA) using ultrasound imaging.
3. Test for correlations between ATMA and LG and MG fiber length, pennation angle, muscle size (volume and PCSA).

The results produced by these aims will be used to test the following hypotheses:

Hypothesis 1:

- There will be a positive correlation between ATMA and fiber length.
    - Prediction: As ATMA increases, fiber length will increase as well.
    - Rationale: Longer ATMA would result in greater fiber excursion, therein increasing contractile velocity for a given joint motion. To maintain

approximately the same operating range of sarcomere length, fiber length would need to increase (Lieber & Fridén, 2000).

Hypothesis 2:

- There will be a negative correlation between ATMA and pennation angle.
    - Prediction: As ATMA increases, plantarflexor pennation angle will decrease.
    - Rationale: Greater pennation angle increases muscle force through greater parallel packing of fibers (Gans, 1982). Therefore, to maintain a joint moment, there would be an inverse relationship between pennation angle and ATMA.

Hypothesis 3:

- There will be a negative correlation between ATMA and muscle size (muscle volume and PCSA).
    - Prediction: As ATMA increases, muscle volume and PCSA will decrease.
    - Rationale: There is evidence that plantarflexion moments scale with body size (Moisio et al., 2003), so joint moments tend to be similar when accounting for variables such as mass and height. Evidence of this scaling suggests that joint moments tend to be only as large as necessary for locomotion. Additionally, if a tendon moment arm is large, then muscle size can be small to achieve joint moments necessary for locomotion. Therefore, I expect there to be an inverse relationship between ATMA and muscle size (muscle volume and PCSA).

Chapter 2

Literature Review

2.1 Overview

The capacity for human musculoskeletal systems to produce joint moments is crucial for locomotor function. Locomotor tasks such as walking, running, and swimming rely on muscles producing sufficient moments about the joints they span. If a human is unable to produce the required muscular joint moments, then they would not be able to move throughout their environment without aid. Dysfunction in the capacity to produce joint moments can be debilitating. This is partly why it has been reported that mobility (represented by walking speed) is positively correlated with health and lifespan (Studenski et al., 2011). Therefore, it is worthwhile to study the basis of muscular joint moments to better understand how those moments contribute to human locomotion. The application of this knowledge has the potential to improve human well-being through better design of orthopedic surgeries, rehabilitation programs, and training programs which consider the factors that contribute to muscular joint moments, and subsequent mobility, such as tendon moment arm and muscle architecture.

2.2 Determinants of Muscular Joint Moment

Many factors contribute to the production of muscular joint moment, including neural drive to the muscle, the resulting muscle force that is produced, and moment arm of the tendon at the joint spanned. A neural stimulus is sent through a motor unit, comprised of a motor nerve and its innervated muscle fibers, which causes tension within the muscle-tendon unit (MTU). The MTU force is applied to a bone and this force produces a moment about a joint center or joint

axis. Production of MTU force is determined by a number of factors which includes fiber activation, muscle force-length/force-velocity relations, optimal fiber length, pennation angle, and muscle size. Some of these factors may be influenced by the moment arm of the MTU about the joint, so that moment arm contributes to joint moment by determining leverage and muscle force simultaneously. Therefore, the remaining sections of this review will focus on factors that contribute to MTU force (fiber contraction mechanics, muscle force-length/force-velocity relations, optimal fiber length, pennation angle, and muscle size), tendon moment arm, and the role of both muscle architecture and tendon moment arm in locomotive function. Lastly, I will discuss the relationship between muscle architecture and tendon moment arm.

2.2.1 Muscle Activation

In this section, I will briefly review the mechanics of fiber contraction and various factors that contribute to skeletal muscle force generation.

The events of muscle contraction are typically initiated by signals sent by the central nervous system to the motor units, which are made up of α-motoneurons and the bundles of muscle cells (muscle fibers) that the motoneurons innervate. Action potentials travel down the peripheral α-motoneurons from the neuronal dendrites, through the cell body, and down the axon to synaptic terminals to the neuromuscular junction (NMJ) through depolarization of the cell membrane that is characterized by the exchange of K^+ ions leaving the nerve and Na^+ ions coming into the nerve. The NMJ is the interface between the presynaptic α-motoneuron axon and the post synaptic fiber membrane.

The neuronal action potential triggers the exchange of Ca^{2+} and acetylcholine across the synaptic cleft to depolarize the sarcolemma (muscle cell membrane), causing a muscle action potential to propagate outwardly from the NMJ (Lieber, 2011). The muscle action potential then propagates deep into the fiber through the transverse tubular system, the T-system, and influences the sarcoplasmic reticulum to release Ca^{2+} to bind to ryanodine receptors. Binding of calcium ions activates the dihydropyridine calcium channel to release calcium into the intracellular fluid around the myofilaments.

The high concentrations of calcium around the myofibrils and sarcomeres leads to a process called the cross-bridge cycle or sliding filament theory, which is the basic of muscle contraction (Geeves et al., 2005; Huxley & Niedergerke, 1954; Huxley & Hanson, 1954). Calcium ions around the myofilaments then bind to troponin on the actin (the thin filament), in the sarcomere, which causes tropomyosin to unveil myosin binding sites. Myosin (the thick filament), which has a phosphate and adenosine diphosphate (ADP) group on it, then sheds its phosphate to "cross-bridge" to the myosin binding site on actin. After forming the cross-bridge, myosin uses stored-up chemical energy to perform a power stroke with actin, which involves the myosin head pivoting to pull actin toward the center of the sarcomere, causing the filaments to slide past each other. Adenosine triphosphate (ATP) then binds to the myosin head to terminate the power stroke by releasing the bond between action and myosin. Next, ATP is hydrolyzed by myosin adenosine triphosphatase (ATPase) into ADP and phosphate. The energy released by this reaction brings the myosin head back into its original position and additional energy is stored in the myosin head. This stored energy is used during the next cycle of this process to perform the power stroke. Together, the processes explained above, from activation of the α-motoneuron to contraction of muscle fibers, are called excitation-contraction (EC) coupling. EC coupling results

in a single muscle twitch (Lieber, 2011). Muscle twitches will continue until actin and myosin are inhibited (relaxation of muscle); this typically occurs when calcium levels are insufficient, or calcium is actively pumped back into the SR by ATPase.

Muscle force generation is further modulated by factors such as temporal summation, motor unit recruitment, and the size principle. EC coupling results in a single muscle twitch when one neuronal impulse initiates it, and this process (excitation -> contraction -> relaxation) takes a finite amount of time to complete. If an additional impulse is received by the fiber before it has relaxed, then the additional impulse is added to the first and results in a greater force. This is called temporal summation. If the frequency of neural impulses is high enough (~40Hz), then fiber relaxation is minimal and force traces become fused, or tetanic (Lieber, 2011). Maximum active tension of skeletal muscle is capable of being achieved when the force trace is tetanic. In other words, fiber tension scales with neuronal impulse frequency. Additionally, muscle force generation scales according to the size principle. The size principle dictates that muscle force increases according to motor unit recruitment that depends on nerve cell size; initially, when lower forces are needed, motor units with smaller axons are recruited, and then, when higher forces are needed, motor units with larger axons are additionally recruited (Henneman et al., 1965). The size principle allows for gradual fluctuations in force, which is thought to be beneficial for fine motor control (Mendell, 2005).

2.2.2 The Force-Length Relation

In this section, I will explain the force-length (F-L) relation of muscle; this description will rely extensively on the previous accounts of Gordon et al. (1966) and Lieber and Ward (2011).

The length of a muscle influences its generation of force, and this relationship has been detailed through animal model studies. Muscle F-L properties have been elucidated through studies conducted across different animal models (Herzog et al., 1992; Moo et al., 2020), but most notably on frog muscle fibers (Gordon et al., 1966; Hill, 1925; Ramsey & Street, 1940). The first description of the F-L relation of individual sarcomeres was provided by Gordon et al. (1966). In this study, the researchers chemically fixated isolated frog muscle fibers with uniform sarcomere lengths. A servomotor was attached to the tendon at one end to adjust fiber length while markers were placed on the fibers to represent striation spacing (sarcomere length). Sarcomere lengths were captured throughout the data collection, while a force transducer was attached to the tendon

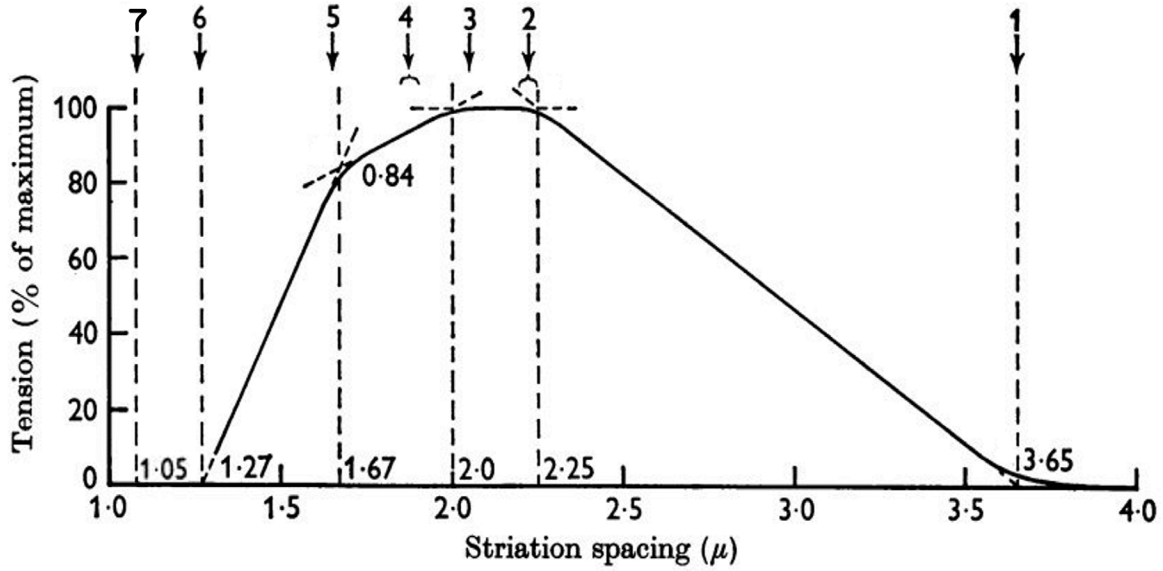

Figure 2-1: The relation between relative muscle tension and sarcomere length in frog with numbers along curve corresponding to events in sliding filament events in **Figure 2-2** (adapted from *Gordon et al. (1966)*).

for tension measurement. The isolated fiber was fully stimulated so maximum isometric tension could be recorded at progressively varied fiber lengths.

The F-L curve from the Gordon et al. (1966) experiment is displayed in **Figure 2-1** with the sliding filament explanation of the shape of the curve in **Figure 2-2** (modified figures from Gordon et al. (1966); see figure captions). Note, this curve represents a fit of data points from several trials from the experiments. **Figure 2-1** shows that maximum tension of frog muscle is produced at an optimal fiber length (region between points 2 and 3 in **Figure 2-1**) when the greatest amount of cross-bridging of myosin and actin occurs (points 2 to 3 in **Figure 2-2**). As sarcomere length decreases from optimum, force decreases precipitously excessive overlap of the filaments occurs, which is represented by the ascending limb, approximately from points 3 to 6 in **Figure 2-1** & **Figure 2-2**; this excessive overlap increasingly disallows cross-bridging of

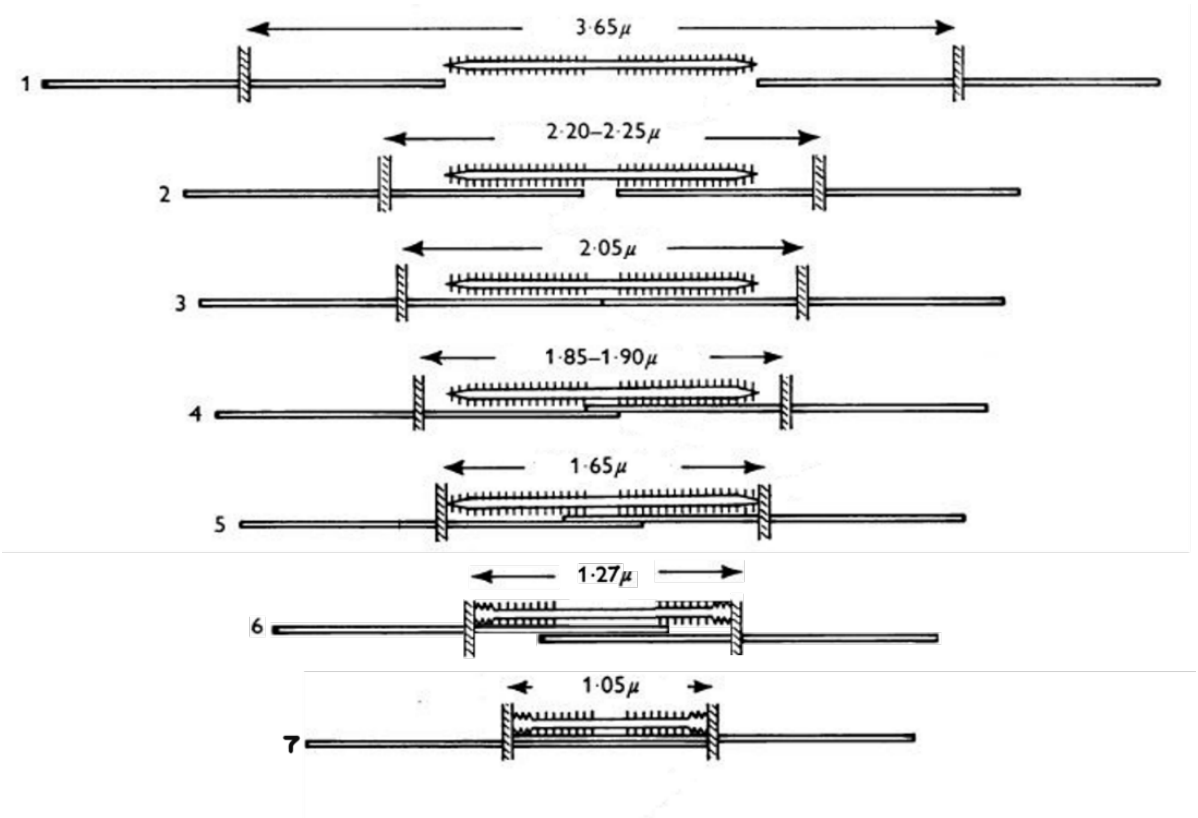

Figure 2-2: Sliding filament overlap events for different sarcomere lengths which refer to numbers along curve in **Figure 2-1** (adapted from *Gordon et al. (1966)*).

myosin and actin until no force can be generated (zero cross-bridges), which occurs from points 6 to 7 (**Figure 2-1** & **Figure 2-2**). Within the region between points 2 and 1 in **Figure 2-1** & **Figure 2-2**, which is known as the descending limb, active force gradually declines as sarcomere lengths increase beyond optimal length until cross-bridge formation is non-existent (zero active force). Moreover, as the fiber lengthens beyond the optimal fiber length, as it does on the descending limb, force drops more gradually as opposed to how force changes on the ascending limb.

The sliding filament theory explains active force production, but it does not explain the passive forces that are also present when muscle fibers are stretched beyond optimal fiber length (Edman et al., 1982; Lieber & Ward, 2011). Passive mechanisms within our fibers, such as the

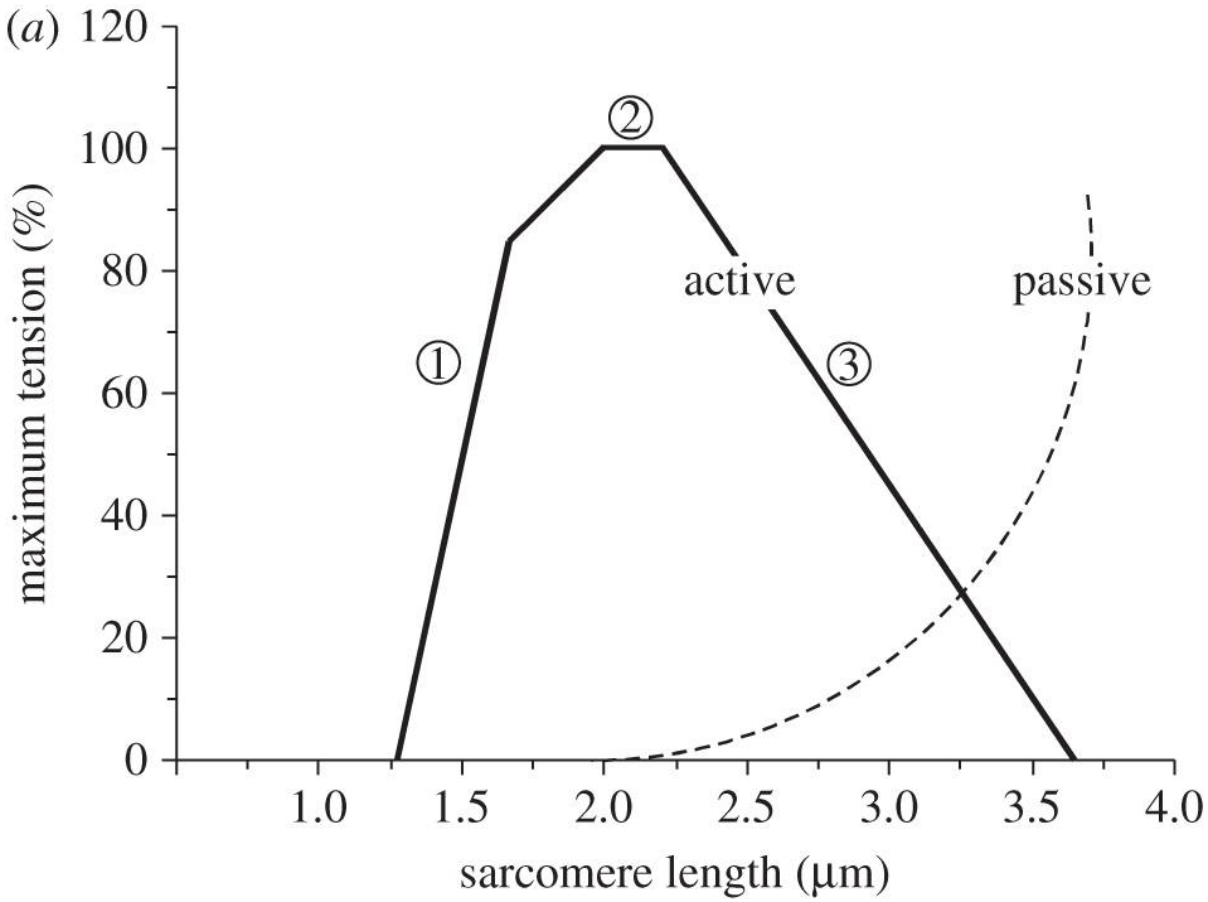

Figure 2-3: Figure from *Lieber and Ward (2011)* depicting the active and passive F-L properties of muscle. This is an idealized F-L curve.

elastic protein called titin, resist lengthening beyond optimal fiber length. As a result, passive force increases exponentially from approximately optimal fiber length to beyond (**Figure 2-3**). Therefore, total force increases as muscle lengthens beyond optimal fiber length (**Figure 2-3**).

2.2.3 The Force-Velocity Relation

The force-velocity (F-V) relation explains how muscle generates force during isotonic contraction. Many studies have shaped our understanding of how muscle force changes with fiber contractile velocity, whether the contraction is concentric (shortening), isometric (length held constant), or eccentric (lengthening) (Edman, 1988; Hill, 1938; Huxley, 1957).

Experiments are conducted in two main ways to construct the F-V relation, represented by a curve showing the maximum active force produced at a given fiber velocity. Experimenters either measure fiber velocity of a maximally activated fiber that is shortening (or lengthening) at a constant tension, or vice versa. Typically, the latter is done by measuring tetanic tension while the fiber length is controlled to cause the fiber to shorten or lengthen at a constant velocity (Hill, 1938). The F-V relation plot is constructed by conducting this procedure at varying velocities (or tensions) to elucidate a trend, similar to how the F-L curve was constructed.

The F-V relation is made up of two portions, the concentric and eccentric curves, which characterize how muscle force changes with velocity (**Figure 2-4**). The units of this relation are generally force and velocity expressed relative to maximum tetanic force and maximum contractile velocity, respectively, as these parameters vary according to the muscle considered. The concentric F-V curve resembles the shape of a rectangular hyperbola (**Figure 2-4**) (Hill, 1938). There is a gradual decline in force as shortening velocity increases (**Figure 2-4**). Reductions in tetanic tension with shortening velocity are due to the rates of attachment and

detachment of cross bridging of actin and myosin. Since these processes have a finite duration, it limits the time over which cross bridges can cycle. Additionally, muscle does not contract as it lengthens, but it produces a relatively large amount of force through its passive properties. Therefore, on the eccentric portion of the F-V relation, muscle force quickly reaches maximum at approximately 150% of peak isometric force as lengthening velocity increases.

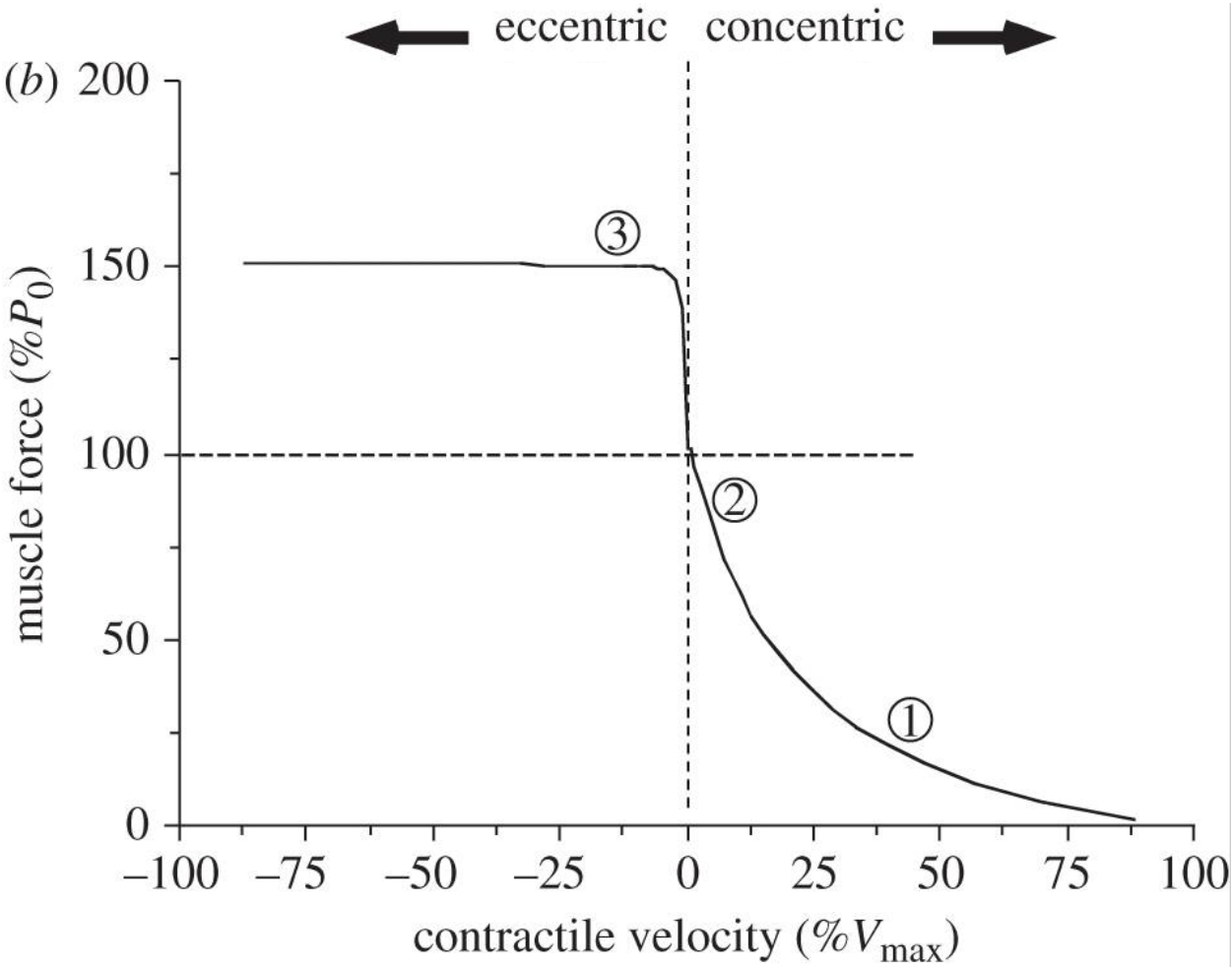

Figure 2-4: Adapted figure from *Lieber and Ward (2011)* showing the relation between relative muscle force and relative contractile velocity, known as the F-V relation of muscle.

2.2.4 Muscle Architecture Affecting Force Generation

Optimal Fiber Length

Since I have already talked in a previous section about optimal fiber length, I will focus on how it determines operating range and responds to kinematic stimuli.

Optimal fiber length characterizes the mechanical properties of the fiber, and there is evidence that optimal fiber length adapts to changes in habitual muscle and joint excursions. It has been suggested that, across animal species, fiber length excursions operate near optimal fiber length during locomotion, and optimal fiber length is often observed at resting muscle length (Burkholder & Lieber, 2001). It has also been reported that human thigh muscles operate near optimal length during locomotion (Cutts, 1989). In immobilization experiments where specimen joint angles were fixed for several weeks and fiber lengths were measured, it was found that sarcomeres are either added or subtracted to accommodate an optimal fiber length near the fixed muscle length (Williams & Goldspink, 1978). Furthermore, Koh and Herzog (1998) found, in a growing rabbit model, that serial sarcomere number increased in response to release of the tibialis anterior (TA) retinaculum, which increased tendon moment arm and muscle excursion. All these findings suggest that muscles might adapt to operate near optimal length during locomotion (or during immobilization).

2.2.4.1 Pennation Angle

Pennation angle is the angular arrangement of fibers with reference to the longitudinal axis of muscle, and it changes throughout joint range of motion, especially under load (Fukunaga et al., 1997). For example, Fukunaga et al. (1997) measured, using ultrasonography, the pennation angle of the vastus lateralis at 10º increments from 110 degrees of knee flexion to full extension,

both passively and actively (10% of maximum isometric voluntary contraction). The researchers determined that pennation angle increased as the muscle shortened, even to a greater degree during the active trials.

Gans (1982) posited that force generating capacity tends to be greater when pennation angle is greater, but the relationship between pennation angle and muscular force is not straight forward. When fibers are arranged at an angle relative to the force generating axis, only a portion of the force is transmitted along the muscle axis for shortening of the muscle; in fact, the transmitted force is equal to $x * \cos(\theta)$, when x is fiber force and θ is pennation angle. When two muscles are identical except in their pennation angle, the muscle with greater pennation would produce less force along the MTU axis than the other (Lieber & Fridén, 2000). Recently, however, Lieber (2022) has argued that pennation angle is best seen as a packing strategy. Although muscle force decreases as pennation angle increases, the increase in pennation angle allows for more fibers to fit in parallel – which may attenuate the force lost due to the fiber axis becoming increasing perpendicular to the MTU axis. Furthermore, since there are spatial limits in body compartments, a greater pennation angle would bias fibers to be shorter. These shorter fibers should reduce contraction velocity and active range of motion. Altogether, greater pennation angle increases force generating capacity by increasing fibers in parallel while reducing contraction velocity through shorter fibers, but this is traded for potentially less active range of motion and a lesser proportion of fiber force transmitted along the MTU axis.

2.2.4.2 Muscle Size

Muscle size is defined in several different ways such as muscle volume, anatomical cross-sectional area (ACSA), and physiological cross-sectional area (PCSA). Muscle volume is the amount of contractile material in a muscle. Additionally, ACSA is the cross-sectional area of muscle perpendicular to the MTU line of action, and PCSA is the cross-sectional area of muscle perpendicular to the fiber line of action.

The volume of muscle affects MTU force and joint moment generation. Theoretically, two muscles can differ in fiber length and PCSA, but if they have the same volume then they will have the same capacity to produce work (force * displacement) and power (force * velocity). Further, positive correlations have been reported between muscle volume and maximum joint moment generation in the elbow extensors and flexors (Fukunaga et al., 2001), plantarflexors (Baxter & Piazza, 2014), and knee extensors (Blazevich et al., 2009), which presents muscle volume as a good anatomical predictor for strength.

Additionally, another indicator of force generating capacity is ACSA. Fiber cross-sectional area is directly related to force generating capacity (Gans & Bock, 1965). The greater the number of myofibrils in parallel, the greater the tension. In a muscle with little to no pennation, ACSA is directly proportional to the sum of the cross-sectional areas of the fibers in the muscle, so ACSA correlates positively with maximum force generation (Gans & Bock, 1965).

However, ACSA varies along the muscle and thus varies in its representation of force generating capacity, so PCSA may be a better indicator (Zajac, 1992). In fact, several studies have suggested that PCSA is one of the best architectural predictors of maximum muscular tension and muscular joint moment (Fukunaga et al., 2001; Gans & de Vree, 1987; Lieber & Fridén, 2000; Lieber & Ward, 2011). With accurate measurements of average fiber length, muscle volume, and

pennation angle, PCSA does not vary based on the site of measurement, unlike ACSA. PCSA defines the cross-sectional area of the fibers in the muscle. The equation for PCSA (**Eq. 2-1**) is as follows, where muscle volume is v_m, pennation angle is θ, and average fiber length is l_F (Powell et al., 1984).

$$PCSA = \frac{v_m * \cos(\theta)}{l_F} \qquad (\mathbf{Eq. 2-1})$$

2.2.5 Tendon Moment Arm

Tendon moment arm, which may be conceptualized as the perpendicular distance from the tendon line of action to the joint axis, is largely a consequence of skeletal geometry (Gans, 1982). It is a variable that tends to change both throughout joint motion and across the lifespan. Tendon moment arm fluctuates with active and passive joint range of motion (Fath et al., 2010; Maganaris, 2004; Rasske et al., 2017). Additionally, recent data suggest there is load dependence between ATMA and joint rotation during walking, especially in younger individuals, which is thought to be due to muscle bulging (Rasske & Franz, 2018). This age reduction in ATMA is likely due to two factors. First, evidence suggests that tendon moment arm decreases with age due to the anterior migration of the AT insertion during aging (Kim et al., 2011). Second, the effects of sarcopenia, age-related muscle tissue degradation, and reductions in neural drive during aging reduce the load dependence of the ATMA.

Tendon moment arm impacts active range of motion, MTU shortening velocity, and generation of muscular joint moment. A longer tendon moment arm will have a greater joint range of motion if there are no confound physiological constraints (Lieber, 2011), and there would be an increase in MTU contractile velocity since excursion is greater. Additionally, when all else is equal, muscular joint moments scale with changes in tendon moment arm.

2.2.6 Fiber Length and Tendon Moment Arm Relation

Considering both tendon moment arm and fiber length determine operation on the F-L and F-V curves, there is reason to look at the ratio of fiber length to moment arm. In fact, in allometric studies of musculoskeletal structure across distinct species, the ratio of fiber length to moment arm is often used to explain the interaction between fiber length, tendon moment arm, and operation on the F-L curve (Crook et al., 2010). Furthermore, the ratio of fiber length to tendon moment arm is useful in determining function in humans (Gans & de Vree, 1987; Lieber & Ward, 2011). When sprinters were compared with non-sprinters, shorter ATMAs and longer fiber lengths of the lateral gastrocnemius were observed in the sprinter group (Lee & Piazza, 2009); this musculoskeletal pairing would allow sarcomeres to operate within a desirable range on the F-L and F-V curves for rapid propulsive movement.

2.2.7 Tendon Moment Arm and Locomotor Function Relation

2.2.7.1 Evidence from Animal Models

A common method to investigate the impact of tendon moment arm on locomotion is with animal models. Biewener (2005) suggested that effective mechanical advantage (EMA), ratio of extensor moment arm to ground force moment arm (r/R), tends to scale with the size of an animal. Larger animals tend to be more erect which decreases the ground force moment arms (increases EMA), and smaller animals tend to be more crouched which increases ground force moment arms (decreases EMA). Having a smaller EMA means that each muscle must exert more force during locomotion, but this is traded off for a better ability to maneuver which is needed for smaller, prey animals (Biewener, 2005). Therefore, EMA seems to be an important factor that contributes to locomotive function across animals.

2.2.7.2 Evidence from Humans

Recent studies suggest that ATMA contributes in complex ways to locomotor function (Baxter & Piazza, 2014; Lee & Piazza, 2012; Rasske et al., 2017; Scholz et al., 2008) As previously mentioned (see above), Lee and Piazza (2009) found shorter ATMAs paired with longer fibers in the lateral gastrocnemius of sprinters when compared with non-sprinters; further, simulations suggested the mechanical leverage lost by having a short ATMA was made up for by operating on a more favorable portion of the F-L and F-V curves of muscle (Lee & Piazza, 2009). This is supported by simulation work by Nagano and Komura (2003), where the researchers found that shorter ATMAs develop greater joint moment, power, and work at fast joint rotations. Similarly, Baxter and Piazza (2014) observed in individuals with shorter ATMAs that ankle joint moment declines to a lesser degree at high speeds of joint rotation.

All these data point to a shorter ATMA being beneficial when force generation is required during rapid shortening, but this requirement is not always the case. For example, when elite Kenyan long-distance runners were compared with Japanese long-distance runners, longer ATMAs were found in the Kenyan group, who tended to perform significantly better (Kunimasa et al., 2014). Furthermore, Lee and Piazza (2012) investigated the relationship between ATMA and walking velocity during a Six Minute Walk Test in elderly subjects. After splitting the group into two, based on walking velocity (faster and slower), a moderately strong positive correlation was found between ATMA and walking velocity in the slower group; although, a weak negative correlation was found between ATMA and walking velocity in the faster group. Clearly, ATMA plays a complicated role in the musculoskeletal system to provide an advantage – or disadvantage – according to specific locomotive tasks within different populations.

2.2.8 Associations between Tendon Moment Arm and Muscle Architecture

2.2.8.1 Evidence from Animal Models

In animal models, there are relations between tendon moment arm and muscle architecture. As mentioned before, Koh and Herzog (1998) observed an increase in TA tendon moment arm after retinacular release in growing rabbits. This increase in TA leverage was coupled with a reduction in the PCSA of the TA and increase in fiber length. However, in adult mice, TA release resulted in a decrease in fiber length and no significant change in TA PCSA (Burkholder & Lieber, 1998). Therefore, it seems there are potential differences in the stimuli that promote musculoskeletal adaptation in muscle across species or developmental stage. Adolescent musculoskeletal systems, especially evidenced in rabbits, could be more sensitive to adapt to the signal of muscle excursion (Crawford, 1954; Koh & Herzog, 1998); while, adult mice musculoskeletal systems might be more sensitive to optimal joint angle whereby maximum tetanic force is produced (Burkholder & Lieber, 1998).

It is likely that tendon moment arm and muscle architecture relations are sensitive to demands of functional muscle groups across species. In support of this claim is the comparative work by McClearn (1985), who compared between racoon and coati the relation of architectural parameters of muscles, according to functional groups, and tendon moment arm. Across these animal models, clear relationships emerged that fiber length is sensitive to tendon moment arm and joint excursions, so fiber length tends to be longer in joint systems which are set up with larger excursions of muscle and joint angles. Additionally, pennation angle, which has a positive correlation with MTU excursion (Gans & Bock, 1965), tended to have a similar relationship as fiber length to excursions of muscle and joint angles but to a smaller degree. Finally, when fiber

lengths were found to be small to moderate in joint systems set up for large excursions, these tended to be biarticular muscles with corollary actions during gait which kept the fiber lengths shorter and within a smaller range (McClearn, 1985). Therefore, it seems that muscle architecture tends to adapt to the functional implications of tendon moment arm and joint dynamics.

2.2.8.2 Evidence from Humans

Recent studies in humans have reported relationships between muscle architecture and tendon moment arm across joint systems (Hori et al., 2020; Maden-Wilkinson et al., 2020; Sugisaki et al., 2010; Sugisaki et al., 2015). In the elbow joint, Sugisaki et al. (2010) found a significant positive correlation between triceps brachii tendon moment arms and ACSA of the triceps brachii. These researchers also observed a slight increase in triceps brachii tendon moment arm after resistance training-induced hypertrophy (increased ACSA) of the triceps brachii (Sugisaki et al., 2015). Additionally, Hori et al. (2020) found a significant position correlation between knee extensor moment arms and force producing capacity, which is defined as knee extensor peak isometric moment divided by quadriceps femoris muscle volume.

Further, in the ankle, it appears that ATMA length is load dependent and, potentially, related to muscle volume but not fascicle length. Rasske et al. (2017) reported that ATMA increases with plantarflexion during walking, as triceps surae muscle bulging increases. This load dependent increase in ATMA tends to be more pronounced in younger subjects when compared to elderly subjects who tend to have sarcopenia (Rasske & Franz, 2018). Additionally, Baxter and Piazza (2014) found a near significant positive relationship between triceps surae muscle volume and ATMA. This relationship between muscle size and ATMA further suggests there could be muscle size effects that impact MTU leverage. However, finally, Maganaris et al.

(2006) found only weak correlations between fascicle length and tendon moment arm within the plantarflexors (lateral gastrocnemius, medial gastrocnemius, and soleus) and knee extensors (vastus lateralis and vastus intermedius). Taken together, there is a complex relationship between muscle architecture and ATMA that primes the musculoskeletal system for specific locomotive domains.

Future research should focus on better understanding structure-function relationships. This knowledge would equip us to better evaluate musculoskeletal profiles which lead to gait pathologies and difficulty with mobility when aging, and to decide if the outcomes from orthopedic surgery protocols and musculoskeletal rehabilitation programs are appropriate.

Chapter 3

Methods

Sixteen healthy participants were recruited for this study (**Table 3-1**). Individuals were excluded from the study if they were under 18 or above 45 years of age, had a history of lower limb musculoskeletal injuries or surgeries, neurological impairments, current ankle and/or foot pain, had a BMI greater than 30 kg/m^2, or competed in elite athletics (college level or higher). Recruitment was completed via a flyer disseminated through a departmental email server list and by word-of-mouth. All research study protocols were approved by the Institutional Review Board (STUDY00020090) at Penn State University.

Table 3-1: Summary of subject characteristics.

Subject Characteristics (9M/7F)		
Parameter	**Male**	**Female**
Age (yrs)	27.64 ± 5.13	27.88 ± 5.30
Stature (m)	1.75 ± 0.03	1.62 ± 0.08
Mass (kg)	76.29 ± 4.36	62.60 ± 15.38
BMI (kg/m^2)	24.79 ± 1.63	23.68 ± 3.67
Shank Length (cm)	40.83 ± 2.54	37.31 ± 3.22
Foot Length (cm)	26.69 ± 0.95	24.34 ± 1.57

Data collection was completed in a single testing session for each participant. Each participant provided informed consent prior to data collection. After informed consent was obtained, height, mass, and date of birth were recorded, followed by shank and foot lengths.

Shank length was defined by the distance from the skin superficial to the lateral tibial condyle to skin superficial to the lateral malleolus, and foot length was measured as the distance from the skin superficial to the posterior aspect of the heel to the skin superficial to the most anterior aspect of the 1st digit. These measurements were taken while the subject was standing in the anatomical position. Lateral and medial gastrocnemius muscle architecture data were then collected along with measurements of Achilles tendon moment arm (see below for details).

3.1 Ultrasound and Motion System Calibration

Prior to data collections, spatial calibration of the ultrasound probe was completed with the single-wall phantom procedure, which has been previously described and validated (Prager et al., 1998), using Stradwin software (v. 6.2, 64bit; Machine Intelligence Laboratory; University of Cambridge, New England, UK). This probe calibration yields homogeneous transformations between the ultrasound image coordinate system and a local probe coordinate system created with the probe markers. This transformation is used later to find the image in the global reference frame. Briefly, this procedure involves rigidly attaching a marker cluster to an ultrasound probe. Then, a set of virtual markers were found within a locally fixed coordinate system to align with the probe imaging plane using a pointer with markers attached to it and a motion system (system detailed below). The virtual markers and coordinate systems can be visualized in **Figure 3-1**.

The probe calibration proceeded as follows. A flat sheet of acrylic was mounted with c-clamps to the bottom of a plastic container measuring approximately 30 cm x 15 cm x 20 cm. This container was filled with room temperature water (~20-22°C). Next, the flat bottom of the container was imaged while the probe was manually moved through a series of prescribed motions during which probe cluster marker trajectories were collected. Care was taken not to

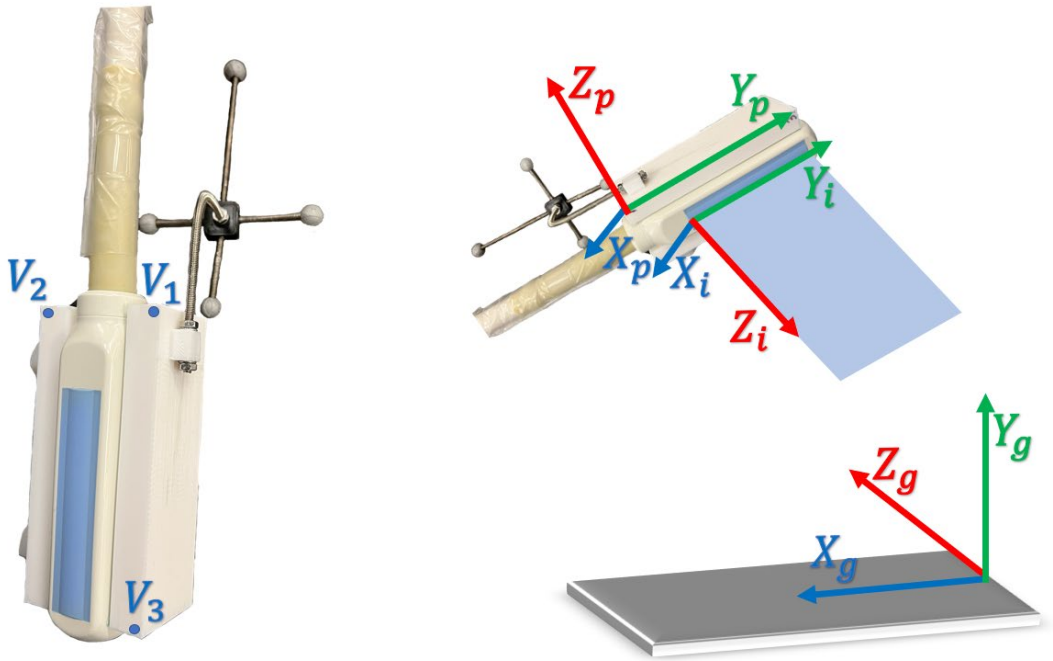

Figure 3-1: The virtual markers (V_1, V_2, & V_3), global coordinate system (defined by X_g, Y_g, & Z_g), probe coordinate system (defined by X_p, Y_p, & Z_p), and image coordinate system (defined by X_i, Y_i, & Z_i) used to find the ultrasound image in the lab space.

submerge the markers throughout these motions. Three vertical translations, three side-to-side rotations, three front-to-back, and three top-to-bottom rotations were performed slowly, using a large range of motion while momentarily pausing at the end of each motion (this momentary pause will be mentioned again below). These motions were then repeated in two additional non-collinear locations in the container to complete one trial. Three trials of these motions were completed.

Ultrasound images were obtained with a 60mm linear ultrasound probe (LV9.0/60/128Z-2) with a B-mode ultrasound machine (30 Hz; LogicScan 128, Telemed, Lithuania; 64-bit Echo Wave II Software, version 4.1.0), synchronized with an 8-camera motion capture system (100 Hz; Cortex, version 8.1.0.2017; Eagle, Motion Analysis Corporation). For synchronization, the offset between the motion and ultrasound data set was determined experimentally. After data collection, marker trajectories were post-processed in Cortex software (version 8.1.0.2017;

Eagle, Motion Analysis Corporation), and motion data were trimmed to be coincident with the ultrasound data. This synchronization was accomplished with the aid of a 5V analog square wave output by the ultrasound beam former and sampled in Cortex. This analog voltage was acquired using a BNC cable connected to the motion system data acquisition board (National instruments PCIe-6259; Austin, TX). Afterwards, the motion and ultrasound data were used to create Stradwin input files with the extensions ".sw" and ".sxi" using a custom-written routine in MATLAB R2022b (Mathworks, Inc; Natick, MA). The file with the extension ".sw" contained textual information including the local probe coordinate system created with the probe markers (see above) and ultrasound data specifications (image resolution, video frame count, etc.). While the file with the ".sxi" extension included binary ultrasound video data.

The Stradwin files was loaded into Stradwin, which used these data to estimate the transformation between the image and probe coordinate systems. In the Stradwin software, the ultrasound images were displayed in a global space, where the user could sift through the ultrasound frames and visualize the motions that the ultrasound imaging plane underwent (**Figure 3-2**). In the probe calibration tab, the offset between the motion and ultrasound data (44 ms) and water temperature (~20-22°C) were specified. Then an arbitrary ultrasound image was digitized to obtain the vertical and horizontal scaling factors (mm per pixel) by clicking on the top left, top right, and bottom left corners of the image. The distances between these clicks (in pixels) were matched to user specified distances in millimeters. The distance from the top left to top right pixel was equivalent to the image width (60mm), and the top left to bottom left pixel distance was equivalent to the imaging depth (50mm).

In the ultrasound image displayed in Stradwin, the container bottom appeared as a white line (**Figure 3-2**). Along this white line were virtual points, equidistant apart, that Stradwin identified with a virtual line running through the cluster of points. Ideally these virtual points would be coincident with the container bottom. Virtual lines were accepted while the probe was at a momentary pause for each motion (refer to description of motion from above). The goal was to only accept virtual lines that were straight (not curved) and coincident with the bottom of the container, and the points that intersected with the line were tightly clustered around the virtual line. If an appropriate virtual line was not found during the momentary pause for a given motion, then no line was accepted for that motion. After all the virtual lines were accepted for each motion, and the coordinates of points along the virtual lines were known, a root mean squares error minimization was completed to find the best transformation between the image and probe coordinate systems. The results of this calibration were employed in two protocols that combined

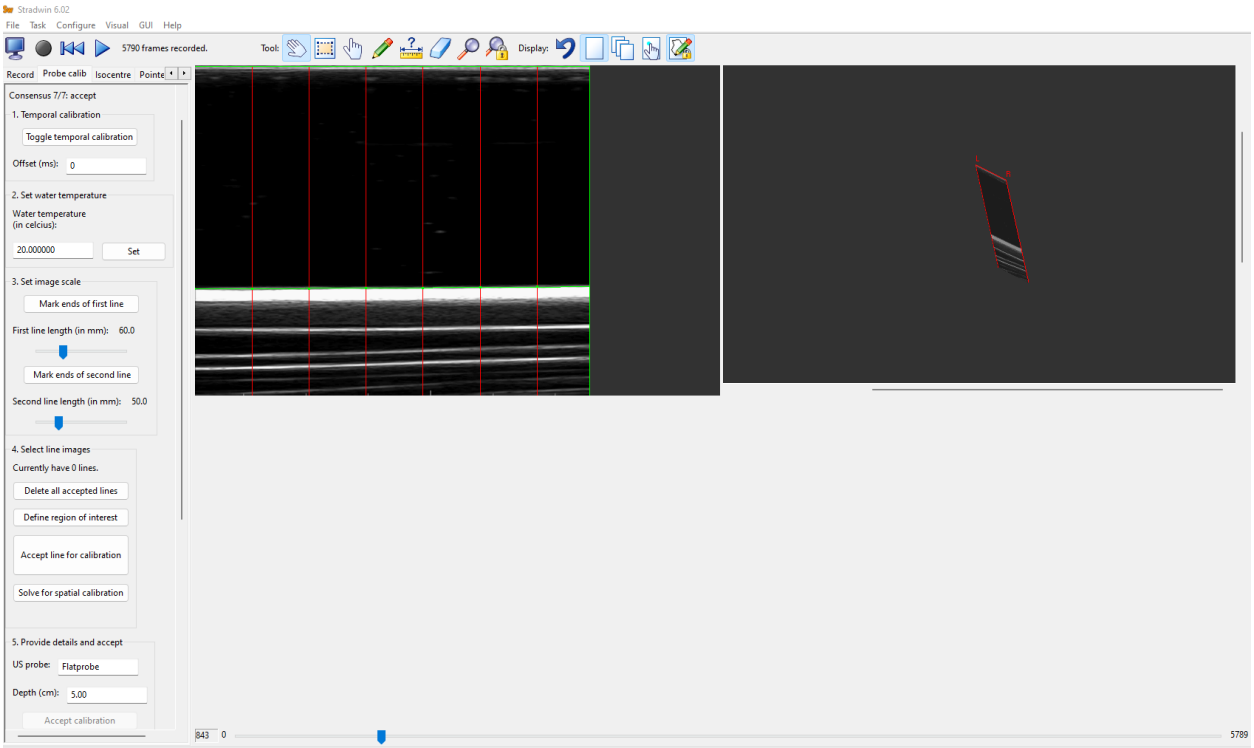

Figure 3-2: Stradwin window displaying the ultrasound video (left) and the ultrasound imaging plane in space (right).

ultrasound imaging with motion analysis – namely, the protocols for the determination of muscle volume and estimation of Achilles tendon moment arm – both of which required finding the global location of an object within the ultrasound image.

3.2 3D Ultrasonography for Muscle Volume

Plantarflexor muscle architecture parameters were measured based on images collected using B-mode ultrasonography and a motion capture system. Participants were instructed to lie prone on an examination table with their right foot extending past the end of the table and the dorsum of the foot aligned with end of table. The leg was positioned with the knee fully extended

Figure 3-3: Gelatin preparation covering the posterior shank to uniformly compress soft tissues therein reducing tissue deformation due to localized probe surface pressure.

and the ankle in neutral position. The right leg was scanned for all participants. A customized gelatin mold (see **Appendix A** for further details) was wrapped around the subject's posterior shank, covering from the superficial aspect of the inferior margin of the medial tibial condyle to approximately two thirds down the shank (**Figure 3-3**). Furthermore, to reduce errors due to positional changes to muscle tissues, the participant was instructed to relax their muscles during testing trials and to remain as still as possible during muscle volume data acquisition. Trials were re-collected if participant movement was detected.

An overlapping set of 2-3 parallel, proximal-to-distal/lateral-to-medial ultrasound image sweeps, approximately ~18 seconds each, were collected over the posterior shank for each gastrocnemius head (LG and MG). Most of the participants' muscles could be imaged in two sweeps, but an additional third sweep was completed with larger muscles to ensure that the entire muscle was scanned. Ultrasound gel was applied both between the skin and gelatin preparation and between the gelatin preparation and the ultrasound interface. Five trials of sets of sweeps of both the LG and MG were collected for muscle volume visualization and acquisition.

Marker trajectories and ultrasound scans were then processed using a MATLAB script. Marker coordinates were filtered with a 4^{th} order low-pass Butterworth filter, with a 25 Hz cut-off frequency. Then Stradwin files were created, as described before, to visualize the ultrasound images in global space (**Figure 3-4B**) but this time for muscle volume acquisition instead of for the calibration. Muscle boundaries were traced to create contours (**Figure 3-4A**) at every 5^{th} frame of the ultrasound images within the sweeps. All contours were completed by one investigator (L. K. Faux-Dugan). In Stradwin, a surface was interpolated through the contours, using maximal disc guided shape based interpolation, to create three-dimensional models of the

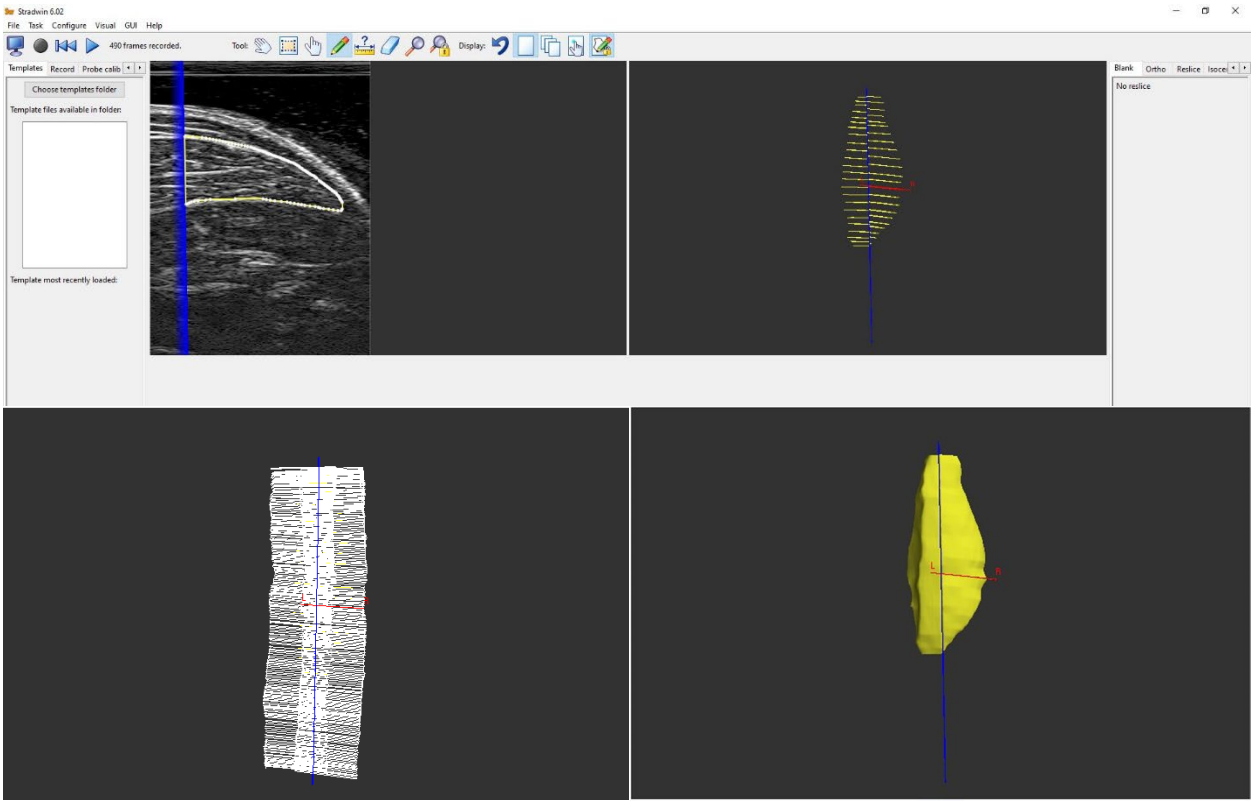

Figure 3-4: A) muscle boundary contours along length of lateral gastrocnemius (top), B) parallel sweep of ultrasound images with blue line representing overlap (bottom left), C) surface interpolation of contours to visualize 3D model of lateral gastrocnemius (bottom right).

lateral and medial gastrocnemius (**Figure 3-4C**) (Treece et al., 1999). Also, muscle volumes were calculated from the contours using cubic planimetry, which is the 3D analog to trapezoidal integration but with cubic interpolation instead of linear interpolation (Treece et al., 1999). Representative muscle volumes were then found by averaging the volumes calculated across the five trials collected for each muscle (LG and MG). Considering factors such as excessive probe scanning pressure and movement of the probe could result in erroneous muscle volume calculations, muscle volume calculations that were considerably different among the muscle volume calculations were not considered in the average calculation.

Pilot tests were completed to establish reliability and accuracy for three-dimensional ultrasound (3DUS) for volume acquisition. Water-filled condom phantoms were imaged using the 3DUS method, similar to Barber et al. (2009). First, each of the condoms were measured to

obtain their weight, and then the condom weight was measured after being filled. The difference between these weights was the volume. The 3DUS method was completed five times on three incrementally sized (small, medium, and large) water-filled condoms and one time on 18 different sized condom phantoms (**Table 3-2**).

Table 3-2: Summary of accuracy and reliability of 3DUS volume measurements

Accuracy and Reliability of Phantom Volume Measurements					
Phantom Size	**Measured Water Volume (cm^3)**	**Estimated Water Volume (cm^3)**	**Difference (cm^3)**	**Percent Error (%)**	**Coefficient of Variation (%)**
Ex: Small	193.3	180.9 ± 0.9	-12.4 ± 0.9	-6.4 ± 0.4	0.5
Ex: Medium	273.5	269.9 ± 0.4	-3.6 ± 0.4	-1.3 ± 0.1	0.1
Ex: Large	330.9	325.5 ± 1.1	-5.4 ± 1.1	-1.6 ± 0.3	0.3
Miscellaneous (18x)	287.5 ± 49.4	282.8 ± 51.3	-4.7 ± 8.8	-1.9 ± 3.3	N/A

The coefficient of variation for five 3DUS measurements of the three phantom sizes, small (193.3 cm^3), medium (273.5 cm^3), and large (330.9 cm^3) were 0.5, 0.1, and 0.3%, respectively (**Table 3-2**). For the 18 phantoms, the average volume was 287.5 ± 49.5 cm^3 and percent errors were -1.9 ± 3.3% (**Table 3-2**).

3.3 3D Ultrasonography for Muscle Volume Apparatus

Originally a custom acrylic container was constructed to make muscle volume measurements with 3DUS, similar to Crouzier et al. (2020), but the design of this container

produced excessive ultrasound reflections off of the sides of the container, rather than dampening these signals. This resulted in ultrasound images with a high noise-to-signal ratio with the ultrasound system used in this study (LV9.0/60/128Z-2; LogicScan 128, Telemed, Lithuania; 64-bit Echo Wave II Software, version 4.1.0). Ultimately, a gelatin preparation was created based on the methods of Thomare et al. (2020) for the ease of use and excellent inter-session, intra-class correlation coefficient, and inter-rater reliability for the measurement of muscle volumes with comparable results to 3DUS with water.

3.4 Estimation of Pennation Angle, Fascicle Length, & PCSA

Several muscle architecture parameters were measured from static ultrasound images taken of the LG and MG. The subject was asked to stand still and upright with their ankles and knees in neutral position for the remaining muscle architecture measurements. Five static ultrasound images were collected in the muscle fascicle plane from the central region of the medial and lateral gastrocnemii. Considering significant errors can arise from attempting to calculate muscle architecture from images misaligned with the muscle fascicle plane, the method proposed by Benard et al. (2009) was followed. First, this entails transverse imaging of the muscle at the distal end of the muscle (approximately mid-shank) and adjusting the probe until the deep aponeurosis was parallel to the bottom of the image. Then, the probe was rotated ~90° to align with the mid-longitudinal axis and gradually moved proximal until within the central region of the muscle (approximately two-thirds of the shank length), where there was close to no curvature of the fascicles and aponeuroses.

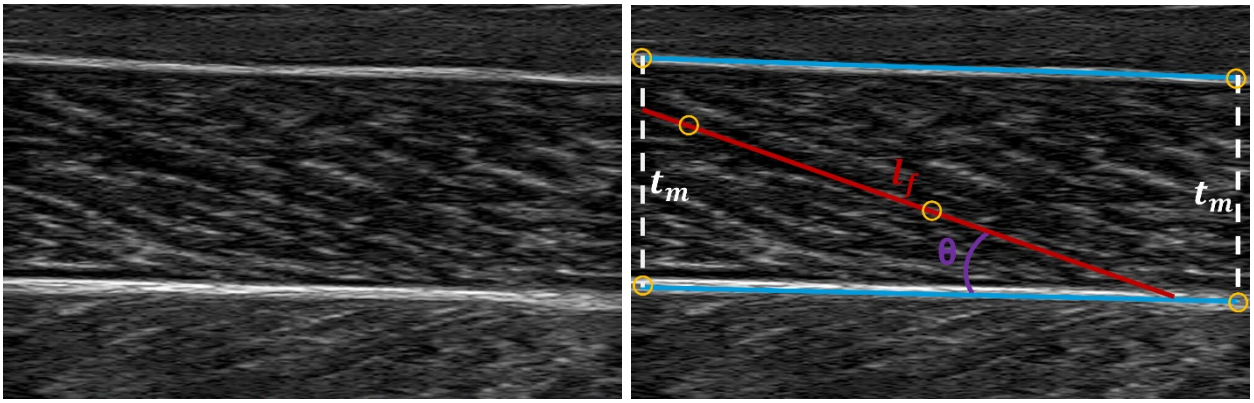

Figure 3-5: Sample ultrasound images of medial gastrocnemius architecture with measurements of muscle thickness, pennation angle, and fascicle length, along with points that were selected on the image.

Using a custom MATLAB script, each ultrasound image of the muscles were analyzed to calculate muscle architecture. First, an image was digitized to find the millimeters per pixel scaling factor. Then, two points were selected on both the superficial and deep aponeuroses and along a representative fascicle (**Figure 3-5**). Muscle thickness, t_m, was calculated as the average vertical distance between the superficial and deep aponeurosis points (Abe et al., 2000; Lee & Piazza, 2009). Pennation angle, θ, was calculated as the acute angle between the fascicle and the deep aponeurosis (Abe et al., 2000; Lee & Piazza, 2009). Fascicle length, l_f, was calculated using **Eq. 3-1** (Abe et al., 2000; Lee & Piazza, 2009). PCSA was calculated using **Eq. 3-2** (Morse et al., 2008). Pixels distances were scaled to represent values in either millimeters or centimeters. All muscle architecture variables were calculated five times from each image, except PCSA. PCSA was calculated from the average variable values from each ultrasound image.

$$l_f = \frac{t_m}{\sin(\theta)} \qquad \textbf{(Eq. 3 - 1)}$$

$$\text{PCSA} = \frac{v_m}{l_f} \qquad \textbf{(Eq. 3 - 2)}$$

3.5 Estimation of Achilles Tendon Moment Arm

Next, data were collected to estimate the Achilles tendon moment arm using the same motion system as describe before but with a low-profile ultrasound probe (LV7.5/60/128Z-2) which can be easily attached to body segments. The ultrasound probe was positioned with plenty of acoustic gel over the skin superficial to the Achilles tendon, slightly above the malleoli and parallel to the tendon line of action. A custom 3D-printed probe case with Velcro straps was utilized to fix the probe within the imaging area. Retroreflective markers were placed on both malleoli, the femoral epicondyles, and a rigid cluster of four markers were mounted on both the dorsal foot and anterior shank (**Figure 3-6**). The individual markers and marker clusters were secured in place using double-sided tape, and elastic wrap when necessary. These procedures are also outline elsewhere in greater detail (Wade et al., 2019).

The participant stood in the center of the motion capture camera system and a static standing motion trial was collected. Then, the participant was instructed to raise onto their toes and lower, in a controlled manner, to a 1 Hz metronome for three cycles. Each trial was approximately six seconds. If requested, a chair was provided for each participant to hold onto for support and balance. The retroreflective marker trajectories and ultrasound images were recorded synchronously while the participant performed their toe raises.

A bidirectional, 4^{th} order low-pass, 10 Hz cut-off frequency, Butterworth filter was used to filter marker trajectories. Utilizing a least squares algorithm, transformations were found between the global and shank and foot coordinate systems (Challis, 1995). Using the relative motion between the shank and foot, a helical axis was computed to represent the ankle joint axis in the shank frame. To find the helical axis at each frame, the relative poses occurring 25 frames before and 25 frames after the frame of interest were considered. A threshold of 0.20 rad for the

minimum magnitude of the helical rotation was set to reduce errors in axes from artifacts associated with skin movement (Woltring et al., 1985); axes associated with smaller movements were discarded from further analysis. The accepted set of finite helical axes were computed in the shank frame and then a single "confluence axode" was calculated to obtain a representative ankle helical axis (Lewis et al., 2006) from this set of axes. A functional finite helical axis was found at each 3D ankle joint angle from decomposed ZXY Cardan angles. Segment reference frames of the foot and shank were conventionalized using ISB recommendations (Wu et al., 2002).

Next, two points along the tendon line of action were found in every frame corresponding to each angle of interest – 0, 5, 10, and 15º of plantarflexion – by locating midpoints on the Achilles tendon via a user-input MATLAB routine. Tendon images were processed to yield images with suitable contrast between the tendon surrounding tissues. A line was created connecting the

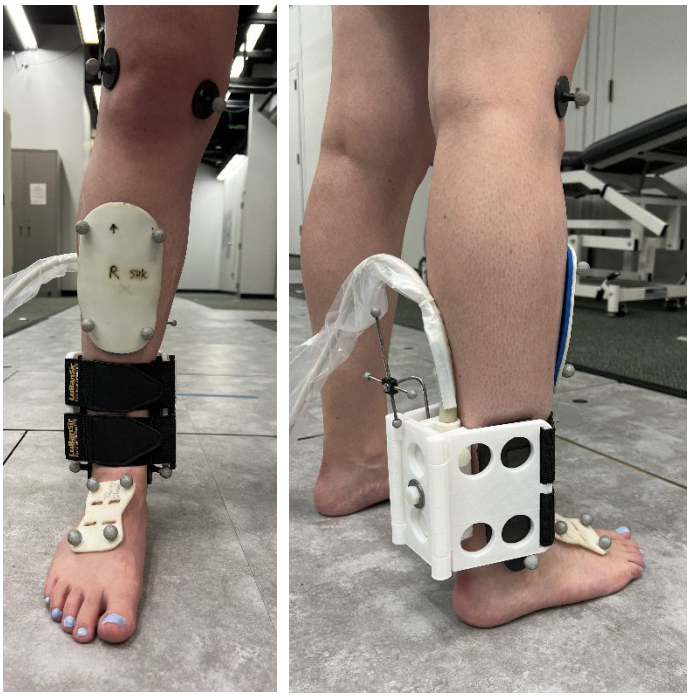

Figure 3-6: Marker and ultrasound probe placement for Achilles tendon moment arm measurement (similar to methods used by *Wade et al. (2019)*).

tendon midpoints, representing the tendon line of action for reference. Every ankle joint angle corresponding to each set of frames, per angle of interest, were within an absolute 1-degree threshold. The midpoint pixel coordinates in the image coordinate system were scaled, using a millimeter per pixel proportionality constant, and transformed into the global frame from the image coordinate system.

Finally, the Achilles tendon moment arm was calculated as described by Wade et al. (2019). First, a vector $\overrightarrow{PQ}$ was computed, pointing from arbitrary points on the helical axis P and the tendon line of action Q. Additionally, a tendon unit force, $\vec{f}$, along the tendon line of action was found. A moment $\overrightarrow{M_p}$ of the tendon unit force about P was taken as the product of $\overrightarrow{PQ}$ and $\vec{f}$ (**Eq. 3-3**).

$$\overrightarrow{M_p} = \overrightarrow{PQ} \times \vec{f} \qquad (\mathbf{Eq.\ 3-3})$$

Next, a unit vector along the length of the helical axis $\vec{u}$ was found by using P and a second arbitrary point along the helical axis P'. Then the component of the moment of the tendon unit force acting along $\vec{u}$, $\overrightarrow{M_{pp'}}$, was calculated as the projection of $\overrightarrow{M_p}$ onto $\vec{u}$ (**Eq. 3-4**).

$$\overrightarrow{M_{pp'}} = \vec{u} \cdot \left(\overrightarrow{PQ} \times \vec{f}\right) \qquad (\mathbf{Eq.\ 3-4})$$

This is given by a scalar triple product: the cross product of $\overrightarrow{PQ}$ and $\vec{f}$ that is in turn dot-multiplied by $\vec{u}$. This triple product was rearranged and the absolute value (to correct for differences in direction between different $\vec{u}$) was taken (**Eq. 3-5**).

$$\text{ATMA} = \left|\overrightarrow{PQ} \cdot \left(\vec{u} \times \vec{f}\right)\right| \qquad (\mathbf{Eq.\ 3-5})$$

3.6 Statistical Analysis

Using MATLAB, simple linear regression models were computed between ATMA (at 0, 5, 10, and 15º of plantarflexion) and muscle architecture parameters (fascicle length, pennation angle, muscle volume, and & PCSA) of both heads of the gastrocnemii (LG & MG). Statistical significance was defined by p-values less than α (α=0.05). Further, a secondary analysis was performed with forward-backward stepwise regression modeling, using the MATLAB function stepwiselm(), to find a reduced model (minimization of sum of squared errors) for the prediction of total muscle volume of the LG and MG. These stepwise regression models included an intercept, linear terms for each predictor – mass, height, ATMA (at either 0, 5, 10, & 15°PF) – and interaction terms for each predictor pair. Additional models were used to predict MVs of the LG and MG with an intercept, linear terms for each predictor – mass, height, ATMA at only 0°PF – and interaction terms for each predictor pair. A predictor was added to the model if the p-value of the F-statistic was less than 0.05 and removed if the p-value was greater than 0.1. Additionally, coefficients of variation were calculated for each measure per subject.

Chapter 4

Results

The repeatability for the measurement of muscle architecture parameters was generally found to be good to excellent. Mean coefficients of variation (CV) for all outcome measures were below 5%, with the highest CV for the measurement of Achilles tendon moment arm (ATMA) at neutral (4.2 ± 1.8%) and lowest CV for the measurement of medial gastrocnemius (MG) pennation angle (PA) (0.9 ± 0.5%) (**Table 4-1**). ATMA increased from 47.5 ± 9.3 at neutral to 51.7 ± 9.5 mm at 15° of plantarflexion (PF) (**Table 4-2**). Reliability was good to excellent for the measurements of ATMA at 5, 10, & 15º of plantarflexion (PF). Average LG and MG fascicles lengths (FLs) were 79.0 ± 14.9 and 60.3 ± 9.0 mm, respectively. Average PAs for the LG were 10.9 ± 2.7°, and average PAs were 18.9 ± 3.4° for the MG. Additionally, mean LG and MG muscle volumes (MVs) taken across subjects were respectively estimated as 128.0 ± 41.0 and 203.2 ± 56.8 cm^3. While values of 16.8 ± 6.4 and 34.3 ± 9.8 cm^2 were derived for physiologic cross-sectional area (PCSA) of the LG and MG, respectively. Correlation coefficients from the regression models between the LG and MG muscle architecture (FL, PA, MV, & PCSA) and ATMA (at 5, 10, & 15°PF) are reported in **Appendix B**.

Table 4-1: Means, SDs, and CVs of ATMA at 0° PF, FL, PA, MV, and PCSA of the LG and MG.

Morphological Parameters		
	Mean ± SD	**Coefficient of Variation (%)**
ATMA, 0° PF (mm)	47.5 ± 9.3	4.2 ± 1.8
FL, LG (mm)	79.0 ± 14.9	1.5 ± 0.7
FL, MG (mm)	60.3 ± 9.0	1.0 ± 0.5
PA, LG (°)	10.9 ± 2.7	1.4 ± 0.7
PA, MG (°)	18.9 ± 3.4	0.9 ± 0.5
MV, LG (cm^3)	128.0 ± 41.0	1.9 ± 0.7
MV, MG (cm^3)	203.2 ± 56.8	1.6 ± 0.8
PCSA, LG (cm^2)	16.8 ± 6.4	10.4 ± 6.6
PCSA, MG (cm^2)	34.3 ± 9.8	8.7 ± 3.1

Table 4-2: Summary of mean ± SD and CV of ATMA at 0, 5, 10, & 15°PF.

Morphological Parameters		
Parameter	**Mean ± SD**	**Coefficient of Variation (%)**
ATMA, 0° PF (mm)	47.5 ± 9.3	4.2 ± 1.8
ATMA, 5° PF (mm)	49.1 ± 9.4	4.0 ± 1.9
ATMA, 10° PF (mm)	50.2 ± 9.7	4.1 ± 1.8
ATMA, 15° PF (mm)	51.7 ± 9.5	3.7 ± 1.9

Table 4-3: Summary of regression correlation coefficients between ATMA at 0°PF and FL, PA, MV, and PCSA of the LG and MG. *Significant correlation (α=0.05)

Regression Correlation Coefficients		
	ATMA, 0° PF (mm)	
	Pearson Correlation Coefficient (R)	p-value (p)
FL, LG (mm)	0.50	**0.049***
FL, MG (mm)	0.23	0.393
PA, LG (°)	0.04	0.894
PA, MG (°)	0.19	0.479
MV, LG (cm^3)	0.62	**0.010***
MV, MG (cm^3)	0.64	**0.008***
PCSA, LG (cm^2)	0.33	0.212
PCSA, MG (cm^2)	0.53	**0.037***
PCSA, MG (cm^2)	0.53	**0.037***

A significant relationship was found between ATMA and LG FL but not between ATMA and MG FL (**Table 4-3**; **Figure 4-1**). A moderate Pearson correlation coefficient (R) of 0.50 was observed for the correlation with ATMA and LG FL with a p-value of 0.049. For the relationship between MG FL and ATMA at neutral, it was weak with an R of 0.23 and p-value of 0.393.

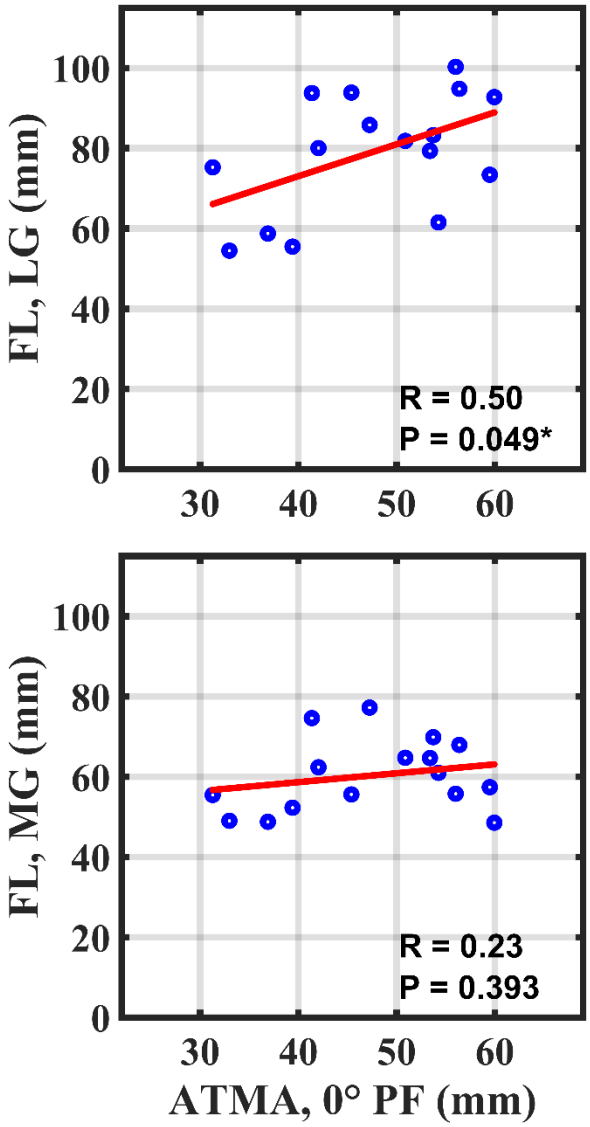

Figure 4-1: Subplots of ATMA vs. FL of the LG (top) and MG (bottom). *Significant correlation (α=0.05)

Correlations between neutral ATMA and PA of the LG and MG were weak and non-significant (**Table 4-3**; **Figure 4-2**). R and p-values for the relationships with ATMA and LG PA were 0.04 and 0.894, respectively; while the respective R and p-values for the relationships with ATMA and MG PA were 0.19 and 0.479.

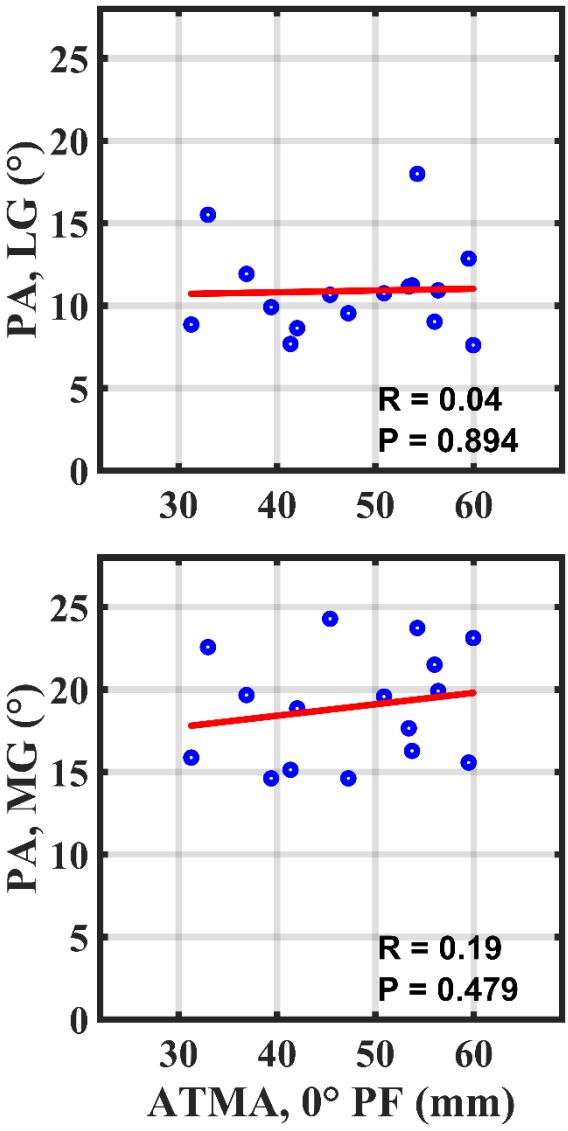

Figure 4-2: Subplots of ATMA vs. PA of the LG (top) and MG (bottom).

Significant moderate correlations were observed between neutral ATMA and MV of the LG and MG (**Table 4-3**; **Figure 4-3**). R values of the relationships between ATMA and MV of the LG and MG were 0.62 and 0.64, respectively, and p-values were 0.010 and 0.008.

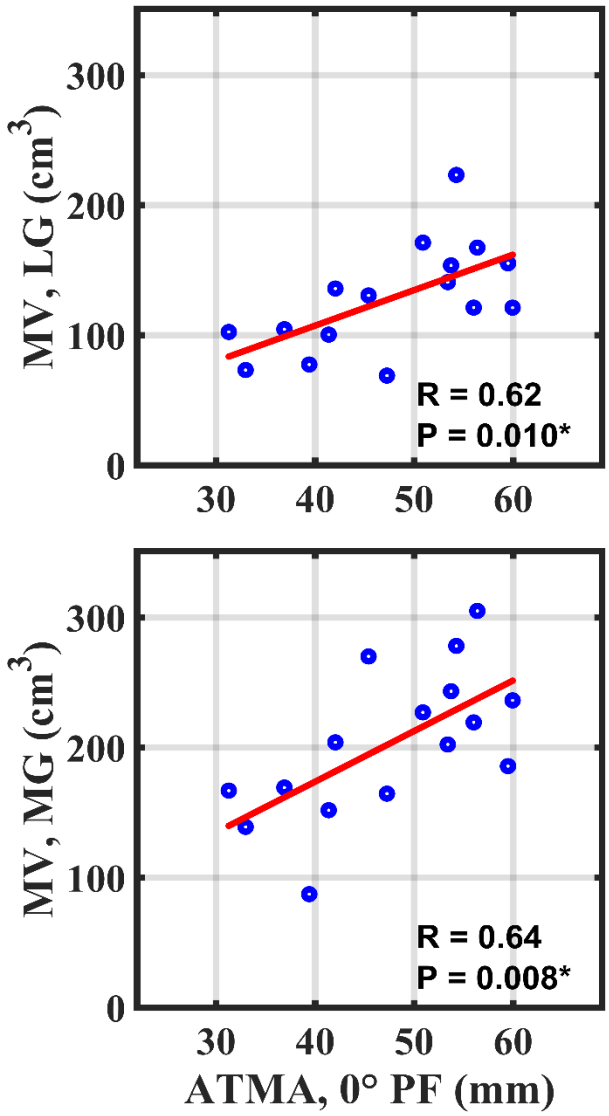

Figure 4-3: Subplots of ATMA vs. MV of the LG (top) and MG (bottom). *Significant correlation (α=0.05)

A significant relationship was found between neutral ATMA and MG PCSA but not between ATMA at neutral and LG PCSA (**Table 4-3**; **Figure 4-4**). A moderate R value of 0.53 was observed for the correlation of ATMA and MG PCSA with a p-value of 0.037. For the relationship between LG PCSA and ATMA at neutral, it was weak with an R of 0.33 and p-value of 0.212.

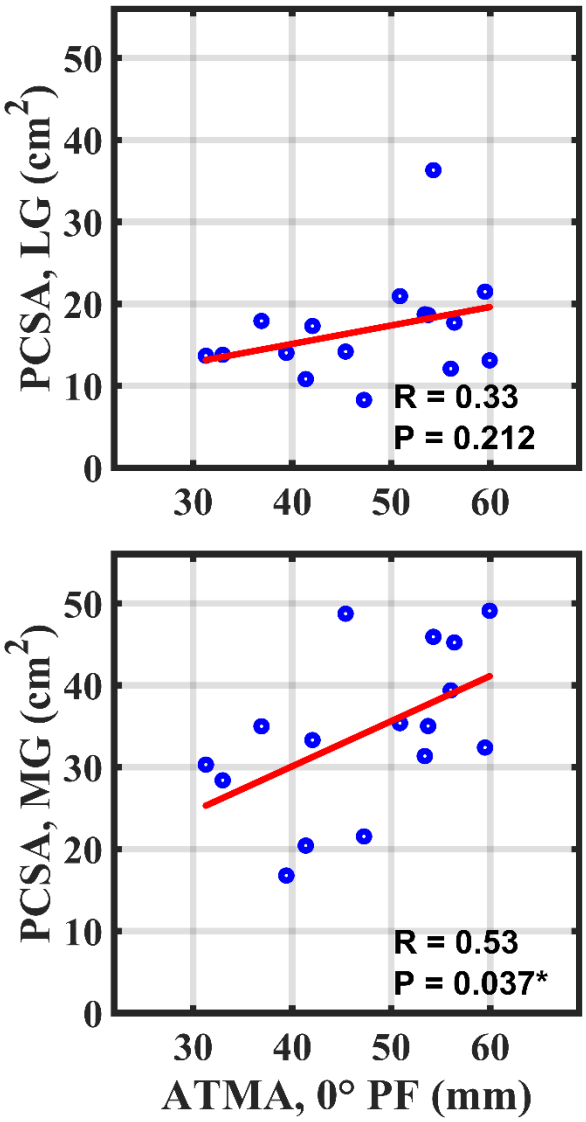

Figure 4-4: Subplots of ATMA vs. PCSA of the LG (top) and MG (bottom). *Significant correlation (α=0.05)

Chapter 5

Discussion

Among the key findings in this thesis are that significant positive correlations were found between Achilles tendon moment arm (ATMA) at 0° of plantarflexion (PF) and the muscle volumes (MVs) of lateral gastrocnemius (LG) and medial gastrocnemius (MG), with p-values of 0.010 (R=0.62) and 0.008 (R=0.64) (**Table 4-3** & **Figure 4-3**). Significant positive, moderate correlations were found between neutral ATMA and LG fascicle length (FL) and MG physiological cross-sectional area (PCSA) with correlation coefficients of 0.50 (p=0.049; **Table 4-3**; **Figure 4-1**) and 0.53 (p=0.037) (**Table 4-3**; **Figure 4-4**). Weak non-significant correlations were observed between ATMA at neutral and pennation angle (PA) of the LG (R=0.04; p=0.894) and MG (R=0.19; p=0.479) (**Table 4-3**; **Figure 4-2**). Additionally, repeatability of all the architectural parameters of muscle were found to be good to excellent (**Table 4-1**).
Several of the findings from this study have not been reported before. To my knowledge, there have not been any in vivo studies where the authors have reported significant positive correlations between ATMA and LG FL, ATMA and MG PCSA, and ATMA and MVs of the LG and MG.

The findings of this study fail to support some, but not all, of the hypotheses. I must reject the hypothesis that there would be a negative correlation between ATMA and muscle size (MV & PCSA) since significant positive correlations were found between ATMA and MV (LG & MG) and MG PCSA, while a non-significant weak positive correlation was observed between ATMA and LG PCSA. The results of non-significant positive correlations between ATMA and PA (LG & MG) rejected the hypothesis that there would be a negative correlation between

ATMA and PA. Additionally, I accept the hypothesis of a positive correlation between ATMA and LG FL, for significant positive correlations were observed between ATMA and LG FL and non-significant weak positive correlations were found between ATMA and MG FL.

The results of this study are comparable to those from similar previous studies. ATMAs were similar in value and varied in a manner that was similar to what was found in previous investigations, as ATMA increased from neutral (47.5 ± 9.3mm) to 15° PF (51.7 ± 9.5 mm) (**Table 4-2**) (Maganaris, 2004; Rasske et al., 2017; Rugg et al., 1990; Wade et al., 2019). FLs of the LG (79.0 ± 14.9mm) and MG (60.3 ± 9.0mm) were comparable to values previously reported by Fouré et al. (2013) (LG, 91.0 ± 31.0mm; MG, 58.0 ± 11mm), Maganaris et al. (1998) (LG, 74.0 ± 3.4mm; MG, 45.0 ± 2.3mm), and Crouzier et al. (2020) (LG, 67.0 ± 8.0mm; MG, 59.0 ± 7.0mm). There was also good agreement between previous data (Crouzier et al., 2020; May et al., 2021) and the PAs from this study (LG, 10.9 ± 2.7°; MG, 18.9 ± 3.4°). Additionally, the average MVs of the LG and MG were found to 128.0 ± 41.0 cm^3 and 203.2 ± 56.8 cm^3, respectively. These averages were slightly less than previously reported by others (Albracht et al., 2008; Barber et al., 2009; Crouzier et al., 2020; Fukunaga et al., 1996; Thomare et al., 2020). Also, in the literature, PCSAs of the LG and MG ranged from 23.2 to 27.8cm^2 and from 41.8 to 51.0cm^2, respectively, and the PCSAs of LG (16.8 ± 6.4cm^2) and MG (34.3 ± 9.8cm^2) of this study varied from the averages of those studies by differences of 8.7 and 12cm^2, respectively (Albracht et al., 2008; Crouzier et al., 2020; Fukunaga et al., 1992; Morse et al., 2008). The small differences observed between the MVs and PCSAs of the present study with previous studies can be explained by factors such as the predominance of male subjects in previous studies (often >80%), unlike the present study (~57%), difference in methods for MV and PCSA estimation, and the inclusion criteria of the present study (i.e., subjects must have had BMI < 30 kg/m^2).

These findings are also supported by the results of others investigating the relationship between tendon moment arm and muscle geometry across joint systems. Like the present study, Baxter and Piazza (2014) reported a positive correlation between ATMA and triceps surae MV, but this relationship only approached significance (p-value = 0.054). Sugisaki et al. (2010) and Sugisaki et al. (2015) reported significant, positive correlations between tendon moment arm and triceps brachii anatomical cross-sectional area (ACSA), which are findings that support the associations that I found between ATMA and muscle size (MG PCSA and MVs of the LG and MG). Additionally, using a cadaver model, Murray et al. (2000) reported strong, significant positive correlations between optimal FLs and peak tendon moment arms across elbow muscles and observed significant positive correlations between peak moment arm and optimal FLs of the brachioradialis and extensor carpi radialis longus. These authors also reported weak non-significant correlations between PCSA and peak tendon moment arm the elbow muscles (Murray et al., 2000). The findings from Murray et al. (2000) also support that there are positive relationships between tendon moment arm and fascicle length of muscles, but their findings were not in support of my findings of positive significant correlations between tendon moment arm and muscle PCSA. However, it should be noted that the muscle-tendon characteristics are different across the ankle plantarflexors and elbow flexors and extensors. Additionally, in opposition to the results of the present study, Maganaris et al. (2006) observed weak, non-significant relationships between tendon moment arm and FLs of the plantarflexors and knee extensors in vivo. Overall, evidence from previous studies tend to support the findings from the present study, but there has been limited research in this area.

There are implications for the correlations found between ATMA and the architecture of the LG and MG. Because it has relatively long FL and small PCSA, the LG is best suited to produce small forces over large MTU excursions. While, the MG, with its relatively small FL and large PCSA, is best suited to produce large forces over small MTU excursions. Larger ATMAs provide more leverage to the plantarflexors but some muscular joint moment production is lost since larger moment arms increase sarcomere contraction velocity; therefore, to reduce sarcomere contraction velocity with larger ATMA, optimal fascicle length would need to increase to keep sarcomeres operating favorably on the F-L and F-V curves, which is what was observed in this study with a significant positive relationship between ATMA at neutral and LG FL (**Table 4-3** & **Figure 4-1**). Additionally, the significant positive relationship between MG PCSA and ATMA implies that the muscular joint moment lost during joint rotations, when ATMA is large, might be mitigated by greater force generating capacity, when PCSA is also large. Furthermore, there was a significant relationship between ATMA and MV of both the LG and MG. This could imply two rationales. First, bigger muscles bulge more and therefore longer ATMAs are associated with larger MVs (Rasske et al., 2017; Sugisaki et al., 2010; Sugisaki et al., 2015). Second, these positive relationships between ATMA and LG and MG muscle architecture are due to size effects between all these parameters (this possibility is discussed further below). Furthermore, the negligible correlations between ATMA and plantarflexor PA may suggest that PA is not a significant feature in musculoskeletal design, as has been proposed recently by Lieber (2022).

The significant positive relationships between ATMA and LG FL, MG PCSA, and MV of the LG and MG could be confounded by body size, but a secondary analysis suggests otherwise. A forward-backward stepwise linear regression model, with interaction terms, was

used to see if ATMA is a uniquely significant predictor of total MV of the LG and MG, V_{LG+MG}, independent from body mass or height. The MATLAB function used for this analysis was stepwiselm() with potential predictors of body mass, height, ATMA at neutral, and interaction terms. The reduced model from the stepwise regression analysis is shown in **Eq. 5-1** (MATLAB output in **Appendix C**). Additionally, this analysis was completed for ATMA at 5, 10, & 15°PF, and, again, to predict MVs of the LG and MG but only with ATMA at 0°PF (MATLAB outputs in **Appendix C**).

$$V_{LG+MG} = 16.42 + 6.62\text{ATMA} \qquad (\textbf{Eq. } \mathbf{5-1})$$

This suggests that ATMA was a significant predictor (p=0.005) of total muscle volume of the LG and MG, independent from body mass or height. However, it should be noted that the findings of stepwise regression models with 2-3 potential predictors are more reliable with observations of approximately 20 or more (only 16 observations in the present study) (Harrell et al., 1984).

There are certain limitations to this study. Though the present protocol for ultrasound of muscle architecture is based on the protocols used in prior studies (Benard et al., 2009; Blazevich et al., 2006; Lee & Piazza, 2009; Maganaris et al., 1998), errors may arise when using this method. Processing images when fascicles extend beyond the ultrasound field of view, or when fascicular and aponeurotic curvature is excessive, can lead to inaccurate estimations of FL and PA (Muramatsu et al., 2002). Additionally, potential errors in FL and PA estimations can come from tissue deformation due to applying excessive probe surface pressure to superficial tissues (Thomare et al., 2020) and misaligning the ultrasound probe with the fascicular plane during imaging (Benard et al., 2009). However, in the present study, excellent repeatability was found from the CVs of the measurements for FLs of the LG (1.5% ± 0.7) and MG (1.0% ± 0.5) and for

the measurements of PA of the LG (1.4% ± 0.7) and MG (0.9% ± 0.5). Furthermore, muscle architecture was measured only in the central region to estimate average FL for a muscle, but muscle geometry varies by region of measurement. However, the central region is often used to capture muscle architecture since FL and PA tend to be more homogenous in this region (Maganaris et al., 1998). Further, the proximal landmark (superficial aspect of the inferior margin of the medial tibial condyle) used for the thee-dimensional ultrasound muscle calculation has been suggested to underestimate muscle volumes by ~11% (Noorkoiv et al., 2019; Thomare et al., 2020), but this ensured there was a standard anatomical landmark that was used across subjects. Additionally, PCSA is a derived parameter which is estimated from measurements of MV and average FL of a muscle, and this derivation imposes an error propagation issue (Blazevich et al., 2009). Blazevich et al. (2009) suggested that ACSA is a better predictor than PCSA of maximum isometric joint moment since it is not derived from estimations of other parameters. Still, PCSA is one of the best predictors of maximum voluntary isometric force, and the values of the present study are comparable to previous data (see above).

Overall, the novel findings of the present study, suggest there are significant positive relationships of neutral ATMA with LG FL, MG PCSA, and MVs of LG and MG. The association that was found between longer ATMAs and larger MVs of the LG and MG corresponds to recent evidence that differences in muscle bulging leads to variation in ATMA (Rasske et al., 2017; Sugisaki et al., 2010; Sugisaki et al., 2015). Furthermore, these findings might suggest the LG, a muscle with a smaller PCSA and longer fascicles, and the MG, a muscle with a larger PCSA and shorter fascicles, might uniquely adapt to ATMA to operate on regions of the F-L and F-V curves that maintain muscular joint moments sufficient for locomotion. However, this hypothesis cannot be addressed by this research. These associations between ATMA and

muscle architecture of the LG and MG could also be determined by genetics or other factors. Future studies should investigate the relationship between ATMA and plantarflexor architecture in different populations to see if similar relationships exist.

BIBLIOGRAPHY

Abe, T., Kumagai, K., & Brechue, W. F. (2000, Jun). Fascicle length of leg muscles is greater in sprinters than distance runners. *Med Sci Sports Exerc, 32*(6), 1125-1129. https://doi.org/10.1097/00005768-200006000-00014

Albracht, K., Arampatzis, A., & Baltzopoulos, V. (2008, Jul 19). Assessment of muscle volume and physiological cross-sectional area of the human triceps surae muscle in vivo. *J Biomech, 41*(10), 2211-2218. https://doi.org/10.1016/j.jbiomech.2008.04.020

Bamman, M. M., Newcomer, B. R., Larson-Meyer, D. E., Weinsier, R. L., & Hunter, G. R. (2000, Jul). Evaluation of the strength-size relationship in vivo using various muscle size indices. *Med Sci Sports Exerc, 32*(7), 1307-1313. https://doi.org/10.1097/00005768-200007000-00019

Barber, L., Barrett, R., & Lichtwark, G. (2009, Jun 19). Validation of a freehand 3D ultrasound system for morphological measures of the medial gastrocnemius muscle. *J Biomech, 42*(9), 1313-1319. https://doi.org/10.1016/j.jbiomech.2009.03.005

Baxter, J. R., & Piazza, S. J. (2014, Mar 1). Plantar flexor moment arm and muscle volume predict torque-generating capacity in young men. *J Appl Physiol (1985), 116*(5), 538-544. https://doi.org/10.1152/japplphysiol.01140.2013

Benard, M. R., Becher, J. G., Harlaar, J., Huijing, P. A., & Jaspers, R. T. (2009, May). Anatomical information is needed in ultrasound imaging of muscle to avoid potentially substantial errors in measurement of muscle geometry. *Muscle Nerve, 39*(5), 652-665. https://doi.org/10.1002/mus.21287

Biewener, A. A. (2005, May). Biomechanical consequences of scaling. *J Exp Biol, 208*(Pt 9), 1665-1676. https://doi.org/10.1242/jeb.01520

Blazevich, A. J., Coleman, D. R., Horne, S., & Cannavan, D. (2009, Apr). Anatomical predictors of maximum isometric and concentric knee extensor moment. *Eur J Appl Physiol, 105*(6), 869-878. https://doi.org/10.1007/s00421-008-0972-7

Blazevich, A. J., Gill, N. D., & Zhou, S. (2006, Sep). Intra- and intermuscular variation in human quadriceps femoris architecture assessed in vivo. *J Anat, 209*(3), 289-310. https://doi.org/10.1111/j.1469-7580.2006.00619.x

Burkholder, T. J., & Lieber, R. L. (1998, Feb). Sarcomere number adaptation after retinaculum transection in adult mice. *J Exp Biol, 201*(Pt 3), 309-316. https://www.ncbi.nlm.nih.gov/pubmed/9503642

Burkholder, T. J., & Lieber, R. L. (2001, May). Sarcomere length operating range of vertebrate muscles during movement. *J Exp Biol, 204*(Pt 9), 1529-1536. https://doi.org/10.1242/jeb.204.9.1529

Cenni, F., Schless, S. H., Bar-On, L., Aertbelien, E., Bruyninckx, H., Hanssen, B., & Desloovere, K. (2018, Mar). Reliability of a clinical 3D freehand ultrasound technique: Analyses on healthy and pathological muscles. *Comput Methods Programs Biomed, 156*, 97-103. https://doi.org/10.1016/j.cmpb.2017.12.023

Cenni, F., Schless, S. H., Monari, D., Bar-On, L., Aertbelien, E., Bruyninckx, H., Hanssen, B., & Desloovere, K. (2018, Aug 22). An innovative solution to reduce muscle deformation during ultrasonography data collection. *J Biomech, 77*, 194-200. https://doi.org/10.1016/j.jbiomech.2018.06.002

Challis, J. H. (1995, Jun). A procedure for determining rigid body transformation parameters. *J Biomech, 28*(6), 733-737. https://doi.org/10.1016/0021-9290(94)00116-l

Crawford, G. N. (1954, May). An experimental study of muscle growth in the rabbit. *J Bone Joint Surg Br, 36-B*(2), 294-303. https://doi.org/10.1302/0301-620X.36B2.294

Crook, T. C., Cruickshank, S. E., McGowan, C. M., Stubbs, N., Wilson, A. M., Hodson-Tole, E., & Payne, R. C. (2010, Jul). A comparison of the moment arms of pelvic limb muscles in horses bred for acceleration (Quarter Horse) and endurance (Arab). *J Anat, 217*(1), 26-37. https://doi.org/10.1111/j.1469-7580.2010.01241.x

Crouzier, M., Tucker, K., Lacourpaille, L., Doguet, V., Fayet, G., Dauty, M., & Hug, F. (2020, May). Force-sharing within the Triceps Surae: An Achilles Heel in Achilles Tendinopathy. *Med Sci Sports Exerc, 52*(5), 1076-1087. https://doi.org/10.1249/MSS.0000000000002229

Cutts, A. (1989, Oct). Sarcomere length changes in muscles of the human thigh during walking. *J Anat, 166*, 77-84. https://www.ncbi.nlm.nih.gov/pmc/articles/PMC1256741/pdf/janat00044-0082.pdf

Edman, K. A. (1988, Oct). Double-hyperbolic force-velocity relation in frog muscle fibres. *J Physiol, 404*, 301-321. https://doi.org/10.1113/jphysiol.1988.sp017291

Edman, K. A., Elzinga, G., & Noble, M. I. (1982, Nov). Residual force enhancement after stretch of contracting frog single muscle fibers. *J Gen Physiol, 80*(5), 769-784. https://doi.org/10.1085/jgp.80.5.769

Fath, F., Blazevich, A. J., Waugh, C. M., Miller, S. C., & Korff, T. (2010, Dec). Direct comparison of in vivo Achilles tendon moment arms obtained from ultrasound and MR scans. *J Appl Physiol (1985), 109*(6), 1644-1652. https://doi.org/10.1152/japplphysiol.00656.2010

Fouré, A., Nordez, A., & Cornu, C. (2013, Mar 1). Effects of eccentric training on mechanical properties of the plantar flexor muscle-tendon complex. *J Appl Physiol (1985), 114*(5), 523-537. https://doi.org/10.1152/japplphysiol.01313.2011

Fukunaga, T., Ichinose, Y., Ito, M., Kawakami, Y., & Fukashiro, S. (1997, Jan). Determination of fascicle length and pennation in a contracting human muscle in vivo. *J Appl Physiol (1985), 82*(1), 354-358. https://doi.org/10.1152/jappl.1997.82.1.354

Fukunaga, T., Kubo, K., Kawakami, Y., Fukashiro, S., Kanehisa, H., & Maganaris, C. N. (2001, Feb 7). In vivo behaviour of human muscle tendon during walking. *Proc Biol Sci, 268*(1464), 229-233. https://doi.org/10.1098/rspb.2000.1361

Fukunaga, T., Roy, R. R., Shellock, F. G., Hodgson, J. A., Day, M. K., Lee, P. L., Kwong-Fu, H., & Edgerton, V. R. (1992, Nov). Physiological cross-sectional area of human leg muscles based on magnetic resonance imaging. *J Orthop Res, 10*(6), 928-934. https://doi.org/10.1002/jor.1100100623

Fukunaga, T., Roy, R. R., Shellock, F. G., Hodgson, J. A., & Edgerton, V. R. (1996, Jan). Specific tension of human plantar flexors and dorsiflexors. *J Appl Physiol (1985), 80*(1), 158-165. https://doi.org/10.1152/jappl.1996.80.1.158

Gans, C. (1982). Fiber architecture and muscle function. *Exerc Sport Sci Rev, 10*, 160-207.

Gans, C., & Bock, W. J. (1965). The functional significance of muscle architecture--a theoretical analysis. *Ergeb Anat Entwicklungsgesch, 38*, 115-142.

Gans, C., & de Vree, F. (1987, Apr). Functional bases of fiber length and angulation in muscle. *J Morphol, 192*(1), 63-85. https://doi.org/10.1002/jmor.1051920106

Geeves, M. A., Fedorov, R., & Manstein, D. J. (2005, Jul). Molecular mechanism of actomyosin-based motility. *Cell Mol Life Sci, 62*(13), 1462-1477. https://doi.org/10.1007/s00018-005-5015-5

Gordon, A. M., Huxley, A. F., & Julian, F. J. (1966, May). The variation in isometric tension with sarcomere length in vertebrate muscle fibres. *J Physiol, 184*(1), 170-192. https://doi.org/10.1113/jphysiol.1966.sp007909

Harrell, F. E., Jr., Lee, K. L., Califf, R. M., Pryor, D. B., & Rosati, R. A. (1984, Apr-Jun). Regression modelling strategies for improved prognostic prediction. *Stat Med, 3*(2), 143-152. https://doi.org/10.1002/sim.4780030207

Henneman, E., Somjen, G., & Carpenter, D. O. (1965, May). Functional Significance of Cell Size in Spinal Motoneurons. *J Neurophysiol, 28*, 560-580. https://doi.org/10.1152/jn.1965.28.3.560

Herzog, W., Leonard, T. R., Renaud, J. M., Wallace, J., Chaki, G., & Bornemisza, S. (1992, Nov). Force-length properties and functional demands of cat gastrocnemius, soleus and plantaris muscles. *J Biomech, 25*(11), 1329-1335. https://doi.org/10.1016/0021-9290(92)90288-c

Hill, A. V. (1925, Sep 4). Length of muscle, and the heat and tension developed in an isometric contraction. *J Physiol, 60*(4), 237-263. https://doi.org/10.1113/jphysiol.1925.sp002242

Hill, A. V. (1938). The heat of shortening and the dynamic constants of muscle. *Proceedings of the Royal Society of London Series B, 126*(843), 136-195. https://doi.org/10.1098/rspb.1938.0050

Hori, M., Suga, T., Terada, M., Miyake, Y., Nagano, A., & Isaka, T. (2020, Jul 20). Torque-producing capacity is affected by moment arm in the human knee extensors. *BMC Res Notes, 13*(1), 343. https://doi.org/10.1186/s13104-020-05182-3

Huxley, A. F. (1957). Muscle structure and theories of contraction. *Prog Biophys Biophys Chem, 7*, 255-318.

Huxley, A. F., & Niedergerke, R. (1954, May 22). Structural changes in muscle during contraction; interference microscopy of living muscle fibres. *Nature, 173*(4412), 971-973. https://doi.org/10.1038/173971a0

Huxley, H., & Hanson, J. (1954, May 22). Changes in the cross-striations of muscle during contraction and stretch and their structural interpretation. *Nature, 173*(4412), 973-976. https://doi.org/10.1038/173973a0

Kim, P. J., Martin, E., Ballehr, L., Richey, J. M., & Steinberg, J. S. (2011, Jan-Feb). Variability of insertion of the Achilles tendon on the calcaneus: an MRI study of younger subjects. *J Foot Ankle Surg, 50*(1), 41-43. https://doi.org/10.1053/j.jfas.2010.10.007

Koh, T. J., & Herzog, W. (1998, Jul). Increasing the moment arm of the tibialis anterior induces structural and functional adaptation: implications for tendon transfer. *J Biomech, 31*(7), 593-599. https://doi.org/10.1016/s0021-9290(98)00052-9

Kunimasa, Y., Sano, K., Oda, T., Nicol, C., Komi, P. V., Locatelli, E., Ito, A., & Ishikawa, M. (2014, Aug). Specific muscle-tendon architecture in elite Kenyan distance runners. *Scand J Med Sci Sports, 24*(4), e269-274. https://doi.org/10.1111/sms.12161

Lee, S. S., & Piazza, S. J. (2009, Nov). Built for speed: musculoskeletal structure and sprinting ability. *J Exp Biol, 212*(Pt 22), 3700-3707. https://doi.org/10.1242/jeb.031096

Lee, S. S., & Piazza, S. J. (2012, Jun 1). Correlation between plantarflexor moment arm and preferred gait velocity in slower elderly men. *J Biomech, 45*(9), 1601-1606. https://doi.org/10.1016/j.jbiomech.2012.04.005

Lewis, G. S., Sommer, H. J., 3rd, & Piazza, S. J. (2006, Aug). In vitro assessment of a motion-based optimization method for locating the talocrural and subtalar joint axes. *J Biomech Eng, 128*(4), 596-603. https://doi.org/10.1115/1.2205866

Lieber, R. L. (2011). *Skeletal muscle structure, function, and plasticity*. Wolters Kluwer Health Adis (ESP).

Lieber, R. L. (2022, Feb). Can we just forget about pennation angle? *J Biomech, 132*, 110954. https://doi.org/10.1016/j.jbiomech.2022.110954

Lieber, R. L., & Fridén, J. (2000, Nov). Functional and clinical significance of skeletal muscle architecture. *Muscle Nerve, 23*(11), 1647-1666. https://doi.org/10.1002/1097-4598(200011)23:11<1647::aid-mus1>3.0.co;2-m

Lieber, R. L., & Ward, S. R. (2011, May 27). Skeletal muscle design to meet functional demands. *Philos Trans R Soc Lond B Biol Sci, 366*(1570), 1466-1476. https://doi.org/10.1098/rstb.2010.0316

Maden-Wilkinson, T. M., Balshaw, T. G., Massey, G. J., & Folland, J. P. (2020, Apr 1). What makes long-term resistance-trained individuals so strong? A comparison of skeletal muscle morphology, architecture, and joint mechanics. *J Appl Physiol (1985), 128*(4), 1000-1011. https://doi.org/10.1152/japplphysiol.00224.2019

Maganaris, C. N. (2004, Mar). Imaging-based estimates of moment arm length in intact human muscle-tendons. *Eur J Appl Physiol, 91*(2-3), 130-139. https://doi.org/10.1007/s00421-003-1033-x

Maganaris, C. N., Baltzopoulos, V., & Sargeant, A. J. (1998, Oct 15). In vivo measurements of the triceps surae complex architecture in man: implications for muscle function. *J Physiol, 512 (Pt 2)*, 603-614. https://doi.org/10.1111/j.1469-7793.1998.603be.x

Maganaris, C. N., Baltzopoulos, V., & Tsaopoulos, D. (2006). Muscle fibre length-to-moment arm ratios in the human lower limb determined in vivo. *J Biomech, 39*(9), 1663-1668. https://doi.org/10.1016/j.jbiomech.2005.04.025

May, S., Locke, S., & Kingsley, M. (2021). Reliability of ultrasonographic measurement of muscle architecture of the gastrocnemius medialis and gastrocnemius lateralis. *PLoS One, 16*(9), e0258014. https://doi.org/10.1371/journal.pone.0258014

McClearn, D. (1985, Jan). Anatomy of raccoon (Procyon lotor) and coati (Nasua narica and N. nasua) forearm and leg muscles: relations between fiber length, moment-arm length, and joint-angle excursion. *J Morphol, 183*(1), 87-115. https://doi.org/10.1002/jmor.1051830106

Mendell, L. M. (2005, Jun). The size principle: a rule describing the recruitment of motoneurons. *J Neurophysiol, 93*(6), 3024-3026. https://doi.org/10.1152/classicessays.00025.2005

Miyake, Y., Suga, T., Otsuka, M., Tanaka, T., Misaki, J., Kudo, S., Nagano, A., & Isaka, T. (2017, Mar). The knee extensor moment arm is associated with performance in male sprinters. *Eur J Appl Physiol, 117*(3), 533-539. https://doi.org/10.1007/s00421-017-3557-5

Moisio, K. C., Sumner, D. R., Shott, S., & Hurwitz, D. E. (2003, Apr). Normalization of joint moments during gait: a comparison of two techniques. *J Biomech, 36*(4), 599-603. https://doi.org/10.1016/s0021-9290(02)00433-5

Moo, E. K., Leonard, T. R., & Herzog, W. (2020, Mar 25). The sarcomere force-length relationship in an intact muscle-tendon unit. *J Exp Biol, 223*(Pt 6). https://doi.org/10.1242/jeb.215020

Morse, C. I., Tolfrey, K., Thom, J. M., Vassilopoulos, V., Maganaris, C. N., & Narici, M. V. (2008, Feb). Gastrocnemius muscle specific force in boys and men. *J Appl Physiol (1985), 104*(2), 469-474. https://doi.org/10.1152/japplphysiol.00697.2007

Muramatsu, T., Muraoka, T., Kawakami, Y., Shibayama, A., & Fukunaga, T. (2002, Jan). In vivo determination of fascicle curvature in contracting human skeletal muscles. *J Appl Physiol (1985), 92*(1), 129-134. https://doi.org/10.1152/jappl.2002.92.1.129

Murray, W. M., Buchanan, T. S., & Delp, S. L. (2000, Aug). The isometric functional capacity of muscles that cross the elbow. *J Biomech, 33*(8), 943-952. https://doi.org/10.1016/s0021-9290(00)00051-8

Nagano, A., & Komura, T. (2003, Nov). Longer moment arm results in smaller joint moment development, power and work outputs in fast motions. *J Biomech, 36*(11), 1675-1681. https://doi.org/10.1016/s0021-9290(03)00171-4

Noorkoiv, M., Theis, N., & Lavelle, G. (2019, Apr). A comparison of 3D ultrasound to MRI for the measurement and estimation of gastrocnemius muscle volume in adults and young people with and without cerebral palsy. *Clin Anat, 32*(3), 319-327. https://doi.org/10.1002/ca.23314

Powell, P. L., Roy, R. R., Kanim, P., Bello, M. A., & Edgerton, V. R. (1984, Dec). Predictability of skeletal muscle tension from architectural determinations in guinea pig hindlimbs. *J Appl Physiol Respir Environ Exerc Physiol, 57*(6), 1715-1721. https://doi.org/10.1152/jappl.1984.57.6.1715

Prager, R. W., Rohling, R. N., Gee, A. H., & Berman, L. (1998, Jul). Rapid calibration for 3-D freehand ultrasound. *Ultrasound Med Biol, 24*(6), 855-869. https://doi.org/10.1016/s0301-5629(98)00044-1

Ramsey, R. W., & Street, S. F. (1940). The isometric length-tension diagram of isolated skeletal muscle fibers of the frog. *Journal of Cellular and Comparative Physiology, 15*(1), 11–34. https://doi.org/https://doi.org/10.1002/jcp.1030150103

Rasske, K., & Franz, J. R. (2018, Aug 22). Aging effects on the Achilles tendon moment arm during walking. *J Biomech, 77*, 34-39. https://doi.org/10.1016/j.jbiomech.2018.06.001

Rasske, K., Thelen, D. G., & Franz, J. R. (2017, Feb). Variation in the human Achilles tendon moment arm during walking. *Comput Methods Biomech Biomed Engin, 20*(2), 201-205. https://doi.org/10.1080/10255842.2016.1213818

Rugg, S. G., Gregor, R. J., Mandelbaum, B. R., & Chiu, L. (1990). In vivo moment arm calculations at the ankle using magnetic resonance imaging (MRI). *J Biomech, 23*(5), 495-501. https://doi.org/10.1016/0021-9290(90)90305-m

Scholz, M. N., Bobbert, M. F., van Soest, A. J., Clark, J. R., & van Heerden, J. (2008, Oct). Running biomechanics: shorter heels, better economy. *J Exp Biol, 211*(Pt 20), 3266-3271. https://doi.org/10.1242/jeb.018812

Studenski, S., Perera, S., Patel, K., Rosano, C., Faulkner, K., Inzitari, M., Brach, J., Chandler, J., Cawthon, P., Connor, E. B., Nevitt, M., Visser, M., Kritchevsky, S., Badinelli, S., Harris, T., Newman, A. B., Cauley, J., Ferrucci, L., & Guralnik, J. (2011, Jan 5). Gait speed and survival in older adults. *Jama, 305*(1), 50-58. https://doi.org/10.1001/jama.2010.1923

Sugisaki, N., Wakahara, T., Miyamoto, N., Murata, K., Kanehisa, H., Kawakami, Y., & Fukunaga, T. (2010, Oct 19). Influence of muscle anatomical cross-sectional area on the moment arm length of the triceps brachii muscle at the elbow joint. *J Biomech, 43*(14), 2844-2847. https://doi.org/10.1016/j.jbiomech.2010.06.013

Sugisaki, N., Wakahara, T., Murata, K., Miyamoto, N., Kawakami, Y., Kanehisa, H., & Fukunaga, T. (2015, Apr). Influence of muscle hypertrophy on the moment arm of the triceps brachii muscle. *J Appl Biomech, 31*(2), 111-116. https://doi.org/10.1123/jab.2014-0126

Thomare, J., Lacourpaille, L., McNair, P. J., Crouzier, M., Ellis, R., & Nordez, A. (2020, Sep 9). A Gel Pad Designed to Measure Muscle Volume Using Freehand 3-Dimensional Ultrasonography. *J Ultrasound Med*. https://doi.org/10.1002/jum.15490

Tomita, D., Suga, T., Ueno, H., Miyake, Y., Otsuka, M., Terada, M., Nagano, A., & Isaka, T. (2018). Relationship between knee extensor moment arm and long-sprint performance in male 400-m sprinters. *Translational Sports Medicine, 1*(4), 172-179. https://doi.org/10.1002/tsm2.33

Treece, G. M., Prager, R. W., Gee, A. H., & Berman, L. (1999, Jun). Fast surface and volume estimation from non-parallel cross-sections, for freehand three-dimensional ultrasound. *Med Image Anal, 3*(2), 141-173. https://doi.org/10.1016/s1361-8415(99)80004-8

Wade, F. E., Lewis, G. S., & Piazza, S. J. (2019, Jun 11). Estimates of Achilles tendon moment arm differ when axis of ankle rotation is derived from ankle motion. *J Biomech, 90*, 71-77. https://doi.org/10.1016/j.jbiomech.2019.04.032

Williams, P. E., & Goldspink, G. (1978, Dec). Changes in sarcomere length and physiological properties in immobilized muscle. *J Anat, 127*(Pt 3), 459-468. https://www.ncbi.nlm.nih.gov/pmc/articles/PMC1235732/pdf/janat00355-0014.pdf

Woltring, H. J., Huiskes, R., de Lange, A., & Veldpaus, F. E. (1985). Finite centroid and helical axis estimation from noisy landmark measurements in the study of human joint kinematics. *J Biomech, 18*(5), 379-389. https://doi.org/10.1016/0021-9290(85)90293-3

Wu, G., Siegler, S., Allard, P., Kirtley, C., Leardini, A., Rosenbaum, D., Whittle, M., D'Lima, D. D., Cristofolini, L., Witte, H., Schmid, O., Stokes, I., Standardization, & Terminology Committee of the International Society of, B. (2002, Apr). ISB recommendation on definitions of joint coordinate system of various joints for the reporting of human joint motion--part I: ankle, hip, and spine. International Society of Biomechanics. *J Biomech, 35*(4), 543-548. https://doi.org/10.1016/s0021-9290(01)00222-6

Zajac, F. E. (1992, Sep). How musculotendon architecture and joint geometry affect the capacity of muscles to move and exert force on objects: a review with application to arm and forearm tendon transfer design. *J Hand Surg Am, 17*(5), 799-804. https://doi.org/10.1016/0363-5023(92)90445-u

Appendix A

Creation of Gelatin Preparation

A shank Cad model was 3D printed to be placed in a gelatin mold. A human body model from GradCAD (grabcad.com) was imported into Rhino, and the shank of this model was cut away to be isolated. This shank section was then scaled to cover the proximal two-thirds of the average shank. Databases such as the NHANES 2013-2016 and ANSUR II were consulted to find the appropriate dimensions (**Figure A1**). The model was 3D printed using PLA.

An acrylic mold was constructed to fit the shank model. This acrylic mold had internal dimensions of 152.4mm (H) x 152.4mm (D) x 305.8mm (L). Acrylic sheets were cut into five smaller sheets since the goal was to create a container with an open top (four side pieces and a base piece). Dimensions of the sheets are in **Table A1**. Sheet edges were smoothed with sanding paper. The 3D printed shank model was glued to the base acrylic sheet aligned with its long axis, and these pieces were left to dry for approximately three hours. Then the walls of the container were chemically welded in place using WELD-ON 3® with an applicator bottle with a needle. C-clamps were utilized to apply pressure between the acrylic pieces to facilitate the solvent welding process. After five minutes, the c-clamps were removed, and the container was left for another two hours. Then, GE® Advanced Silicone sealant was applied to all the acrylic container cracks to ensure it was waterproof.

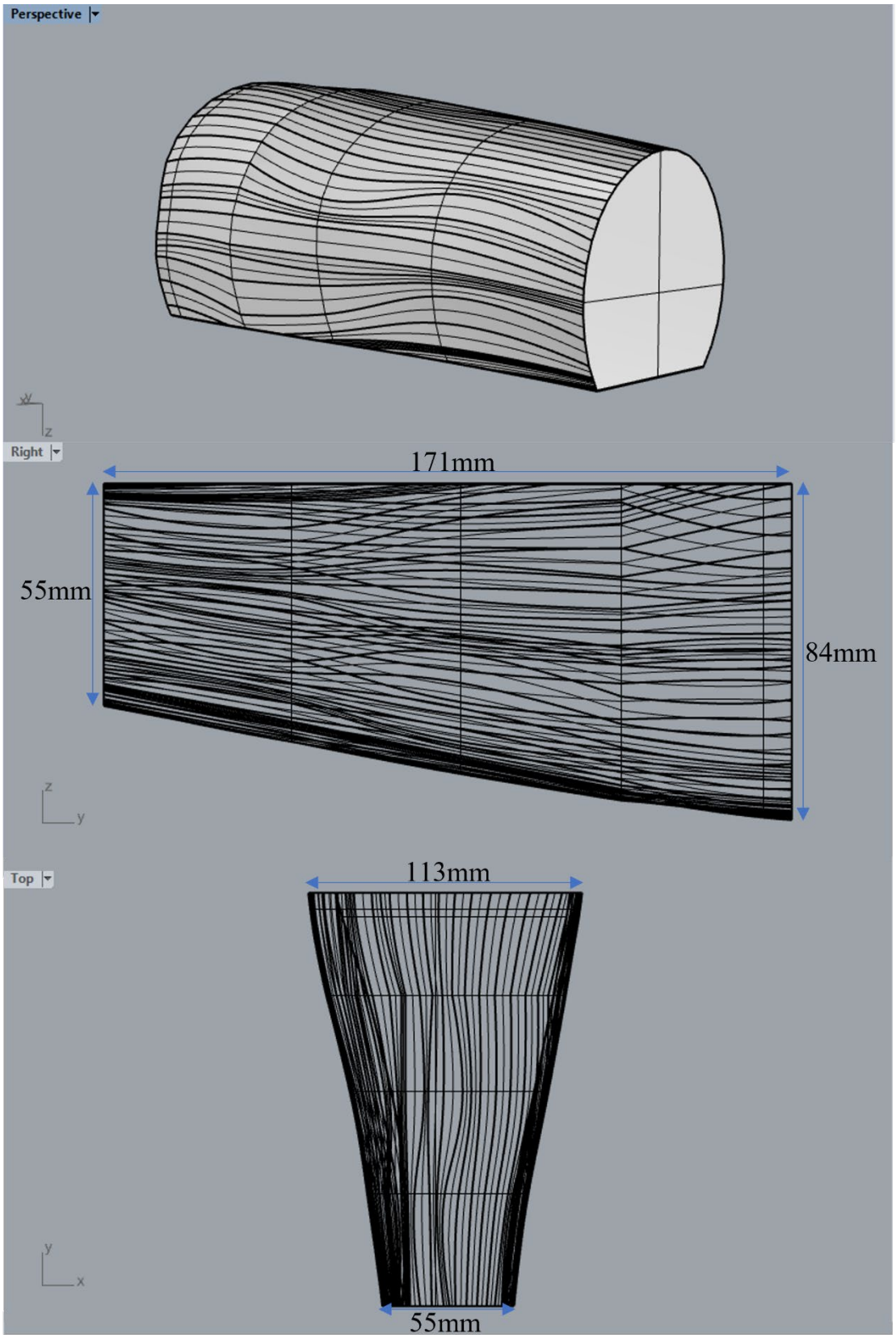

Figure A1: Shank model dimensions in Rhino software.

Table A1: Dimensions of container acrylic sheets

Container Sheet Dimensions	
Quantity	**Dimensions**
2x	11.1mm (H) x 152.4mm (D) x 304.8mm (L)
2x	11.1mm (H) x 152.4mm (D) x 174.6mm (L)
1x	11.1mm (H) x 174.6mm (D) x 327.0mm (L)

The gelatin ingredients were prepared, weighed, mixed, and left to bloom. 3120g of water was weighed and then left in a 16 qt. pot in a fridge for two hours to reduce its temperature from room temperature (20-22 °C) to approximately 4 °C. While the water was reducing in temperature, 1g of crystalized thymol was mixed into 60g of 70% isopropyl alcohol until the crystals were dissolved. After the water was to an appropriate temperature, 810g of Knox powdered porcine gelatin was weighed and then slowly poured into the cold water in intervals of small quantities while the water was stirred. Care was taken to ensure the gelatin was dissolved before adding more. Then the 1g, thymol:60g, 70% isopropyl alcohol solution and 60g of glycerin were added, and the mixture was left for three hours to "bloom." Blooming refers to letting the gelatin mixture settle and partially solidify. This process ensures that the gelatin has a smooth texture after it is heated to be poured into the mold.

After blooming, the gelatin was heated and then poured into the mold. The gelatin needed to be heated gradually over approximately 30 minutes to not burn the gelatin. Gelatin on the edges of the pot were prone to becoming burnt, which would disrupt the texture and properties of the gelatin. Therefore, the temperature was continuously stirred and monitored throughout this process. The 16 qt. pot with the gelatin mixture was first placed into a sink of hot water to slowly

raise the temperature. If the water become cold, then the water was replaced with hot water. After the temperature of the mixture reached 37°C, the pot was moved to a portable induction stove top set to 60°C. The pot was removed from the stove after the gelatin reached 50°C. The gelatin mixture was then poured into the mold, which was lined with non-stick spray to facilitate de-molding. The mold and mixture were covered and left to solidify overnight.

The next morning, the gelatin preparation had solidified, and it was removed from the mold by breaking the seals of one of the side walls of the mold with a mallet. This gelatin preparation was then placed in a large plastic bag, sealed with zip ties, and stored away from UV light in a container within a temperature-controlled room at room temperature (20-22°C).

This gelatin preparation was originally developed by Thomare et al. (2020) in response to errors associated with using 3D ultrasound (3DUS), which is the reconstruction of 3D volumes from 2D ultrasound images, for the estimation of muscle volumes. 3DUS with the gelatin preparation has been suggested to reduce the non-uniform, local pressure applied to the superficial tissues during imaging that led to errant calculations of muscle volume (Barber et al., 2009; Cenni, Schless, Bar-On, et al., 2018; Cenni, Schless, Monari, et al., 2018; Thomare et al., 2020).

Appendix B

Correlations between Muscle Architecture and ATMA at 5, 10, & 15°PF

Significant positive moderate correlations were found between LG FL and ATMA at 5 and 10° PF with correlation coefficients of 0.53 (p-value=0.00.035) for both (**Table B1**; **Figure B1**). All correlations between the PAs, for LG and MG, and ATMA at all angles of PF were weak and non-significant (**Table B1**; **Figure B2**). Significant positive correlations were found between muscle volume (MV) of the LG and ATMA at 5 (R=0.61, p=0.012), 10 (R=0.62, p=0.011), & 15° PF (R=0.63, p=0.012); also, significant positive correlations were found between MV of the MG and ATMA at 5 (R=0.62, p=0.011), 10 (R=0.62, p=0.011), & 15° PF (R=0.61, p=0.016) (**Table B1**; **Figure B3**). Additionally, a significant moderate, positive relationship was observed between MG PCSA and ATMA at 15ºPF (R=0.52, p=0.049), but the remaining correlations between PCSAs and ATMAs were weak and non-significant (**Table B1**; **Figure B4**).

Table B1: Summary of regression models between ATMA at 0, 5, 10, & 15°PF and FL, PA, MV, and PCSA of the LG and MG. *Significant p-value ($\alpha<0.05$)

	Regression Models					
	ATMA, 5° PF (mm)		**ATMA, 10° PF (mm)**		**ATMA, 15° PF (mm)**	
Parameter	**R**	**p**	**R**	**p**	**R**	**p**
FL, LG (mm)	0.53	**0.035***	0.53	**0.035***	0.45	0.091
FL, MG (mm)	0.28	0.301	0.28	0.285	0.18	0.511
PA, LG (°)	-0.01	0.969	-0.02	0.939	0.01	0.971
PA, MG (°)	0.15	0.580	0.13	0.635	0.16	0.576
MV, LG (cm^3)	0.61	**0.012***	0.62	**0.011***	0.63	**0.012***
MV, MG (cm^3)	0.62	**0.011***	0.62	**0.011***	0.61	**0.016***
PCSA, LG (cm^2)	0.30	0.252	0.31	0.246	0.36	0.183
PCSA, MG (cm^2)	0.49	0.055	0.48	0.060	0.52	**0.049***

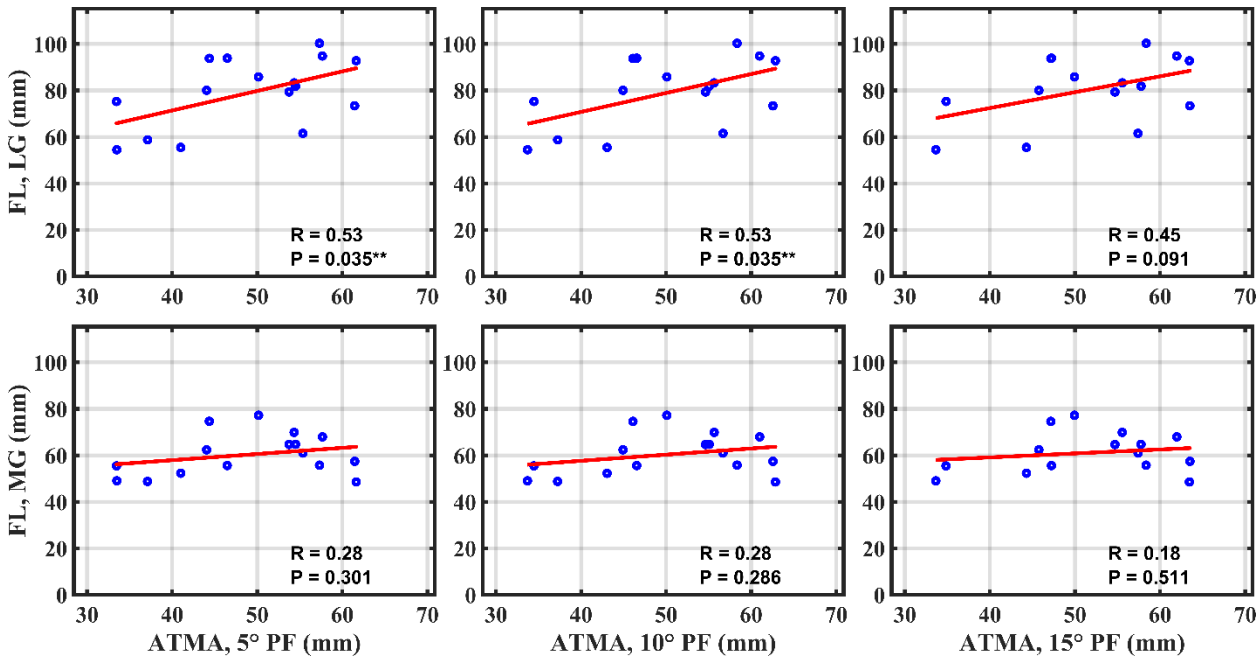

Figure B1: Subplots of correlations between FL (LG & MG) and ATMA at 5, 10, & 15ºPF. *Significant p-value ($\alpha<0.05$)

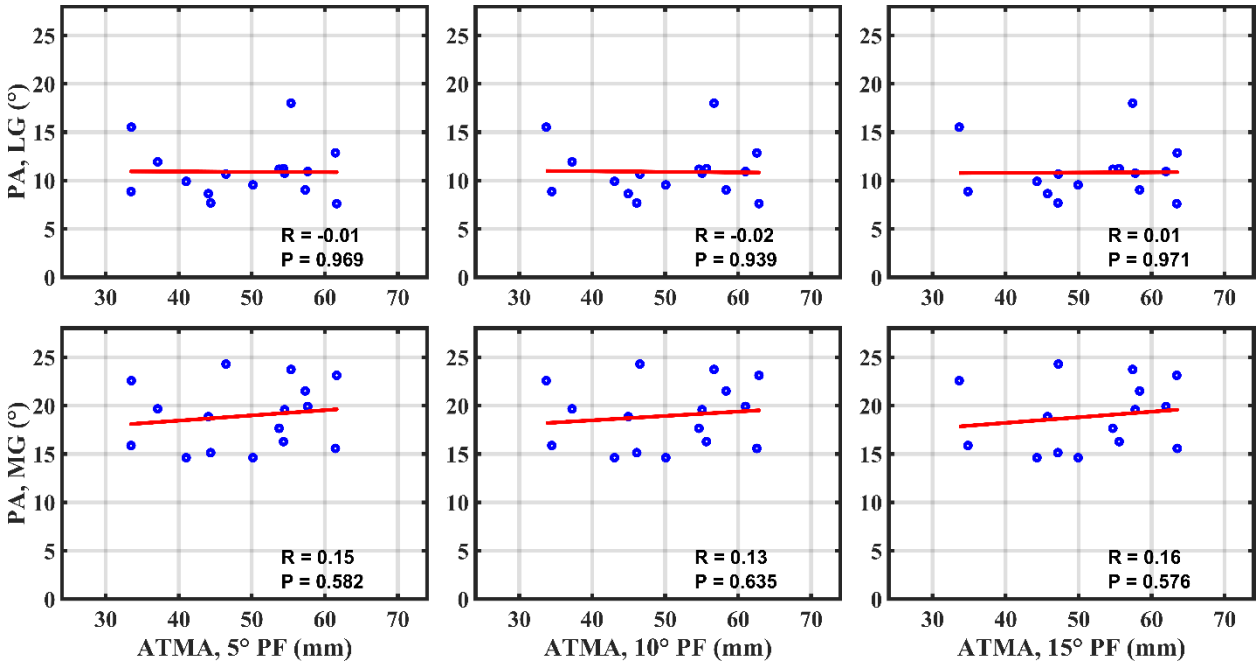

Figure B2: Subplots of correlations between PA (LG & MG) and ATMA at 5, 10, & 15ºPF. *Significant p-value ($\alpha<0.05$)

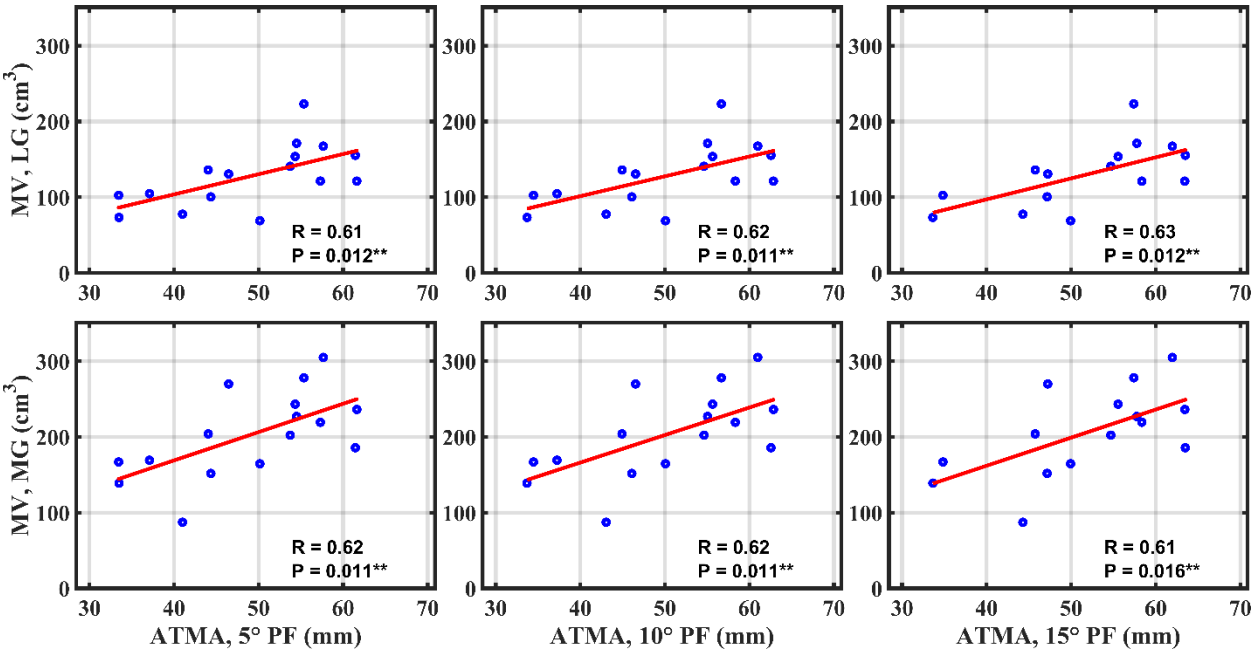

Figure B3: Subplots of correlations between MV (LG & MG) and ATMA at 5, 10, & 15ºPF. *Significant p-value ($\alpha<0.05$)

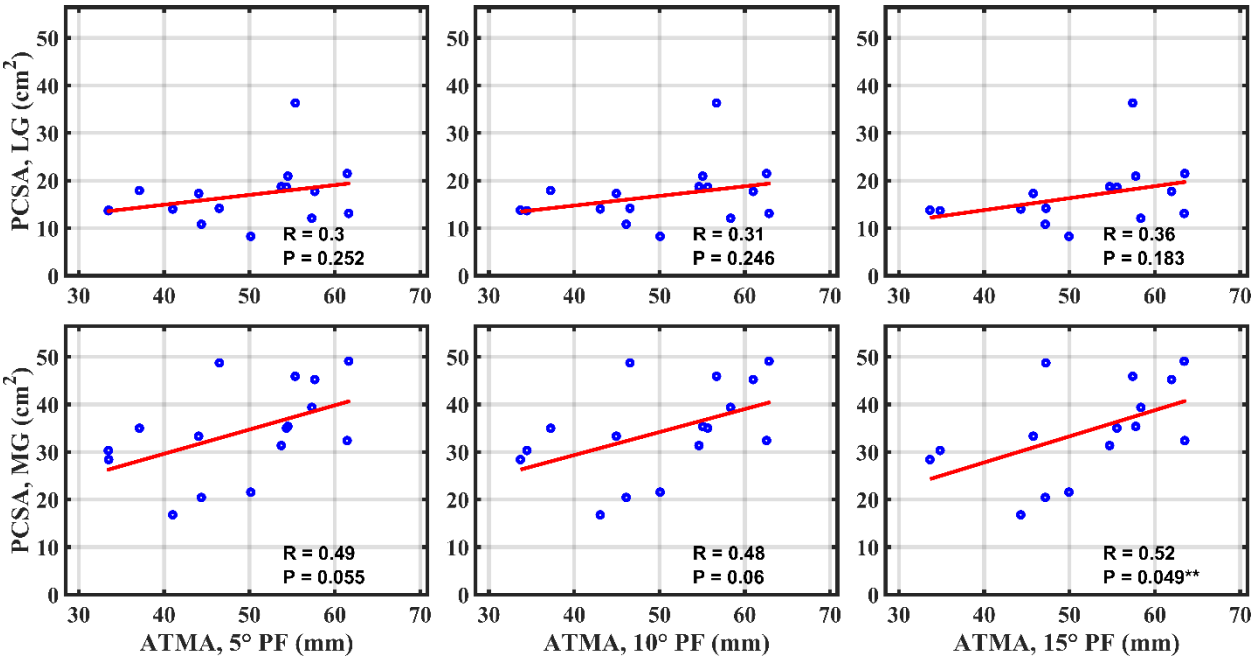

Figure B4: Subplots of correlations between PCSA (LG & MG) and ATMA at 5, 10, & 15ºPF. *Significant p-value ($\alpha<0.05$)

Appendix C

MATLAB Output for Stepwise Regression Models

Forward-backward stepwise regression modeling was performed, using the MATLAB function stepwiselm(), to find a reduced model (minimization of sum of squared errors) for the prediction of total muscle volume of the LG and MG. These stepwise regression models included an intercept, linear terms for each predictor – mass, height, ATMA (at either 0, 5, 10, & 15°PF) – and interaction terms for each predictor pair. Additional models were used to predict MVs of the LG and MG with an intercept, linear terms for each predictor – mass, height, ATMA at only 0°PF – and interaction terms for each predictor pair. A predictor was added to the model if the p-value of the F-statistic was less than 0.05 and removed if the p-value was greater than 0.1. Tables defining the MATLAB variables and figures displaying the MATLAB outputs for the stepwise regression models can be found below.

Table C1: MATLAB variable definitions for model 1.

MATLAB Variable Definitions for Model 1	
Variable	**Definition**
m	Body mass
h	Height
ma0	ATMA at neutral
mvLG	Muscle volume of LG
h:m	Product of height and body mass (interaction term)
h:ma0	Product of height and ATMA at neutral (interaction term)
m:ma0	Product of body mass and ATMA at neutral (interaction term)
model_mvLG_intmh0	Reduced model that minimized root mean squared error with candidate predictors of body mass, height, ATMA at neutral, and interactions terms

```
   No candidate terms to add
   pValue for removing h:m is 0.94923
   pValue for removing h:ma0 is 0.97273
   pValue for removing m:ma0 is 0.3852
1. Removing h:ma0, FStat = 0.0012356, pValue = 0.97273
   No candidate terms to add
   pValue for removing h:m is 0.91571
   pValue for removing m:ma0 is 0.32237
2. Removing h:m, FStat = 0.011782, pValue = 0.91571
   pValue for adding h:ma0 is 0.92883
   pValue for removing h is 0.73514
   pValue for removing m:ma0 is 0.081008
3. Removing h, FStat = 0.1204, pValue = 0.73514
   No candidate terms to add
   pValue for removing m:ma0 is 0.073177

model_mvLG_intmh0 =


Linear regression model:
    mvLG ~ 1 + m*ma0

Estimated Coefficients:
                   Estimate       SE        tStat      pValue
                   ________    ________    _______    ________

    (Intercept)     439.21       251.55      1.746     0.10633
    m              -5.4741       3.6301     -1.508     0.15743
    ma0            -11.137       6.4962    -1.7144     0.11215
    m:ma0          0.17682     0.090049     1.9636    0.073177


Number of observations: 16, Error degrees of freedom: 12
Root Mean Squared Error: 27.9
R-squared: 0.629,  Adjusted R-Squared: 0.536
F-statistic vs. constant model: 6.77, p-value = 0.00636
```

Figure C1: MATLAB output for model 1

Table C2: MATLAB variable definitions for model 2.

MATLAB Variable Definitions for Model 2	
Variable	**Definition**
m	Body mass
h	Height
ma0	ATMA at neutral
mvMG	Muscle volume of MG
h:m	Product of height and body mass (interaction term)
h:ma0	Product of height and ATMA at neutral (interaction term)
m:ma0	Product of body mass and ATMA at neutral (interaction term)
model_mvMG_intmh0	Reduced model that minimized root mean squared error with candidate predictors of body mass, height, ATMA at neutral, and interactions terms

```
   No candidate terms to add
   pValue for removing h:m is 0.58766
   pValue for removing h:ma0 is 0.26713
   pValue for removing m:ma0 is 0.96605
1. Removing m:ma0, FStat = 0.0019148, pValue = 0.96605
   No candidate terms to add
   pValue for removing h:m is 0.54344
   pValue for removing h:ma0 is 0.19399
2. Removing h:m, FStat = 0.39566, pValue = 0.54344
   pValue for adding m:ma0 is 0.83623
   pValue for removing m is 0.18577
   pValue for removing h:ma0 is 0.093757
3. Removing m, FStat = 1.9921, pValue = 0.18577
   No candidate terms to add
   pValue for removing h:ma0 is 0.1824
4. Removing h:ma0, FStat = 2.0032, pValue = 0.1824
   pValue for adding m is 0.43078
   pValue for removing h is 0.13171
   pValue for removing ma0 is 0.10242
5. Removing h, FStat = 2.5876, pValue = 0.13171
   pValue for adding m is 0.095781
   pValue for removing ma0 is 0.007778

model_mvMG_intmh0 =


Linear regression model:
    mvMG ~ 1 + ma0

Estimated Coefficients:
                   Estimate      SE       tStat      pValue
                   ________    ______    _______    ________

    (Intercept)      18.187     60.667    0.29979     0.76874
    ma0              3.8907     1.2536     3.1035    0.007778


Number of observations: 16, Error degrees of freedom: 14
Root Mean Squared Error: 45.3
R-squared: 0.408,  Adjusted R-Squared: 0.365
F-statistic vs. constant model: 9.63, p-value = 0.00778
```

Figure C2: MATLAB output for model 2

Table C3: MATLAB variable definitions for model 3.

MATLAB Variable Definitions for Model 3	
Variable	**Definition**
m	Body mass
h	Height
ma0	ATMA at neutral
mvtotal	Total muscle volume of LG and MG
h:m	Product of height and body mass (interaction term)
h:ma0	Product of height and ATMA at neutral (interaction term)
m:ma0	Product of body mass and ATMA at neutral (interaction term)
model_mvtotal_intmh0	Reduced model that minimized root mean squared error with candidate predictors of body mass, height, ATMA at neutral, and interactions terms

```
   No candidate terms to add
   pValue for removing h:m is 0.69588
   pValue for removing h:ma0 is 0.46427
   pValue for removing m:ma0 is 0.6443
1. Removing h:m, FStat = 0.16294, pValue = 0.69588
   No candidate terms to add
   pValue for removing h:ma0 is 0.5127
   pValue for removing m:ma0 is 0.72815
2. Removing m:ma0, FStat = 0.1278, pValue = 0.72815
   pValue for adding h:m is 0.8173
   pValue for removing m is 0.10485
   pValue for removing h:ma0 is 0.071972
3. Removing m, FStat = 3.1237, pValue = 0.10485
   No candidate terms to add
   pValue for removing h:ma0 is 0.186
4. Removing h:ma0, FStat = 1.968, pValue = 0.186
   pValue for adding m is 0.29762
   pValue for removing h is 0.12482
   pValue for removing ma0 is 0.071271
5. Removing h, FStat = 2.6918, pValue = 0.12482
   pValue for adding m is 0.062306
   pValue for removing ma0 is 0.0047328

model_mvtotal_intmh0 =


Linear regression model:
    mvtotal ~ 1 + ma0

Estimated Coefficients:
                   Estimate      SE       tStat      pValue
                   ________    ______    _______    _________

    (Intercept)      16.427     95.539    0.17194      0.86595
    ma0              6.6203     1.9743     3.3533    0.0047328


Number of observations: 16, Error degrees of freedom: 14
Root Mean Squared Error: 71.3
R-squared: 0.445,  Adjusted R-Squared: 0.406
F-statistic vs. constant model: 11.2, p-value = 0.00473
```

Figure C3: MATLAB output for model 3

Table C4: MATLAB variable definitions for model 4.

MATLAB Variable Definitions for Model 4	
Variable	**Definition**
m	Body mass (predictor)
h	Height (predictor)
ma5	ATMA at 5°PF (predictor)
mvtotal	Total muscle volume of LG and MG (response)
h:m	Product of height and body mass (interaction term)
h:ma5	Product of height and ATMA at 5°PF (interaction term)
m:ma5	Product of body mass and ATMA at 5°PF (interaction term)
model_mvtotal_intmh5	Reduced model that minimized root mean squared error with candidate predictors of body mass, height, ATMA at 5°PF, and interactions terms

```
   No candidate terms to add
   pValue for removing h:m is 0.93991
   pValue for removing h:ma5 is 0.76329
   pValue for removing m:ma5 is 0.5597
1. Removing h:m, FStat = 0.0060086, pValue = 0.93991
   No candidate terms to add
   pValue for removing h:ma5 is 0.75382
   pValue for removing m:ma5 is 0.51638
2. Removing h:ma5, FStat = 0.10392, pValue = 0.75382
   pValue for adding h:m is 0.95373
   pValue for removing h is 0.43507
   pValue for removing m:ma5 is 0.07631
3. Removing h, FStat = 0.65623, pValue = 0.43507
   No candidate terms to add
   pValue for removing m:ma5 is 0.089508

model_mvtotal_intmh5 =


Linear regression model:
    mvtotal ~ 1 + m*ma5

Estimated Coefficients:
                   Estimate      SE        tStat      pValue
                   ________    _______    _______    ________

    (Intercept)      926.1      561.72     1.6487     0.12512
    m               -11.101     8.1512    -1.3619     0.19825
    ma5             -21.846     13.846    -1.5777     0.14061
    m:ma5           0.35757    0.19357     1.8472    0.089508


Number of observations: 16, Error degrees of freedom: 12
Root Mean Squared Error: 59.5
R-squared: 0.669,  Adjusted R-Squared: 0.587
F-statistic vs. constant model: 8.1, p-value = 0.00324
```

Figure C4: MATLAB output for model 4

Table C5: MATLAB variable definitions for model 5.

MATLAB Variable Definitions for Model 5	
Variable	**Definition**
m	Body mass (predictor)
h	Height (predictor)
ma10	ATMA at 10°PF (predictor)
mvtotal	Total muscle volume of LG and MG (response)
h:m	Product of height and body mass (interaction term)
h:ma10	Product of height and ATMA at 10°PF (interaction term)
m:ma10	Product of body mass and ATMA at 10°PF (interaction term)
model_mvtotal_intmh10	Reduced model that minimized root mean squared error with candidate predictors of body mass, height, ATMA at 10°PF, and interactions terms

```
   No candidate terms to add
   pValue for removing h:m is 0.87216
   pValue for removing h:ma10 is 0.80234
   pValue for removing m:ma10 is 0.49171
1. Removing h:m, FStat = 0.027411, pValue = 0.87216
   No candidate terms to add
   pValue for removing h:ma10 is 0.82773
   pValue for removing m:ma10 is 0.46715
2. Removing h:ma10, FStat = 0.0499, pValue = 0.82773
   pValue for adding h:m is 0.93685
   pValue for removing h is 0.45636
   pValue for removing m:ma10 is 0.070087
3. Removing h, FStat = 0.59605, pValue = 0.45636
   No candidate terms to add
   pValue for removing m:ma10 is 0.080407

model_mvtotal_intmha10 =


Linear regression model:
    mvtotal ~ 1 + m*ma10

Estimated Coefficients:
                   Estimate      SE        tStat      pValue
                   ________    _______    _______    ________

    (Intercept)     924.28      544.52     1.6974     0.11538
    m              -11.054      7.8506    -1.408      0.18451
    ma10           -21.246      13.089    -1.6231     0.13052
    m:ma10         0.34777     0.18214     1.9094    0.080407


Number of observations: 16, Error degrees of freedom: 12
Root Mean Squared Error: 58.4
R-squared: 0.681,  Adjusted R-Squared: 0.601
F-statistic vs. constant model: 8.54, p-value = 0.00263
```

Figure C5: MATLAB output for model 5

Table C6: MATLAB variable definitions for model 6.

MATLAB Variable Definitions for Model 6	
Variable	**Definition**
m	Body mass (predictor)
h	Height (predictor)
ma15	ATMA at 15°PF (predictor)
mvtotal	Total muscle volume of LG and MG (response)
h:m	Product of height and body mass (interaction term)
h:ma15	Product of height and ATMA at 15°PF (interaction term)
m:ma15	Product of body mass and ATMA at 15°PF (interaction term)
model_mvtotal_intmh15	Reduced model that minimized root mean squared error with candidate predictors of body mass, height, ATMA at 15°PF, and interactions terms

```
   No candidate terms to add
   pValue for removing h:m is 0.77271
   pValue for removing h:ma15 is 0.58019
   pValue for removing m:ma15 is 0.27031
1. Removing h:m, FStat = 0.089281, pValue = 0.77271
   No candidate terms to add
   pValue for removing h:ma15 is 0.56358
   pValue for removing m:ma15 is 0.23223
2. Removing h:ma15, FStat = 0.35949, pValue = 0.56358
   pValue for adding h:m is 0.77527
   pValue for removing h is 0.34806
   pValue for removing m:ma15 is 0.081017
3. Removing h, FStat = 0.96935, pValue = 0.34806
   No candidate terms to add
   pValue for removing m:ma15 is 0.089912

model_mvtotal_intmh15 =


Linear regression model:
    mvtotal ~ 1 + m*ma15

Estimated Coefficients:
                   Estimate      SE        tStat      pValue
                   ________    _______    _______    ________

    (Intercept)     953.22       571.3     1.6685      0.1234
    m              -11.674      8.5671    -1.3627     0.20023
    ma15           -21.482      13.328    -1.6117     0.13531
    m:ma15         0.35437     0.19059     1.8594    0.089912


Number of observations: 15, Error degrees of freedom: 11
Root Mean Squared Error: 59.9
R-squared: 0.684,  Adjusted R-Squared: 0.598
```

Figure C6: MATLAB output for model 6